



PONTIFICIA UNIVERSIDAD CATOLICA DE CHILE  
ESCUELA DE INGENIERIA

# **PERFORMANCE OF ADVANCED TRIPLE-JUNCTION (ATJ) SOLAR CELLS**

**ROLF ALLAN LÜDERS MORALES**

Memoria para optar al título de  
Ingeniero Civil Electricista

Profesor Supervisor:  
ANDRÉS GUESALAGA MEISSNER

Santiago de Chile, 2005



PONTIFICIA UNIVERSIDAD CATOLICA DE CHILE  
ESCUELA DE INGENIERIA  
Departamento de Ingeniería Eléctrica

# **PERFORMANCE OF ADVANCED TRIPLE-JUNCTION (ATJ) SOLAR CELLS**

**ROLF ALLAN LÜDERS MORALES**

Memoria presentada a la Comisión integrada por los profesores:

**ANDRÉS GUESALAGA MEISSNER**

**JUAN DIXON ROJAS**

**ÁLVARO SOTO ARRIAZA**

Para completar las exigencias del título de  
Ingeniero Civil Electricista

Santiago de Chile, 2005

## ACKNOWLEDGEMENTS

I would like to express my gratitude to Francisco Calderón, classmate and friend with whom we participated in the Life in the Atacama project representing Pontificia Universidad Católica de Chile. This work is the result of many hours of discussions as part of our long-run teamwork to complete our respective theses. Both complementary works are the result of a common goal, which was to accurately characterize new ATJ solar technologies. This made us work together on both of our theses.

I want to thank the Department of Electrical Engineering of the Pontifical Catholic University of Chile for allowing me to carry-out this research, specially to my professor and advisor Andrés Guesalaga, who was always aware of my work and was at all times available when I needed his advice. I also want to show my appreciation to him for trusting in me and allowing me to participate in the Life in the Atacama project, which has opened many professional possibilities.

I have to give special credit to James Teza, electrical engineer of the Field Robotics Center at Carnegie Mellon University (CMU), for his help in searching for specialized documents and papers relevant for this work. David Wettergreen, Michael Wagner, and the rest of the Life in the Atacama team from the Robotics Institute of CMU, merit particular gratitude for their unconditional support.

## CONTENTS

	Pág.
ACKNOWLEDGEMENTS .....	ii
LIST OF TABLES .....	v
LIST OF FIGURES.....	vi
RESUMEN.....	ix
ABSTRACT .....	x
1 INTRODUCTION .....	1
1.1 Objectives.....	1
2 TECHNICAL BACKGROUND .....	3
2.1 Semiconductor Basics .....	3
2.1.1 Semiconductor Doping .....	5
2.1.2 P-N Junction Operation .....	9
2.1.3 Isolated P-N Junction .....	10
2.1.3 Forward and Reverse Bias .....	12
2.2 Photovoltaic Cell Operation.....	15
2.2.1 Separation of Charge .....	16
2.2.2 Isolated Photocell.....	17
2.2.3 Photocell with Load .....	17
2.3 Design Considerations .....	18
2.4 Multi-Junction Solar Cells .....	19
2.4.1 Construction Procedure .....	19
2.4.2 Advanced Triple Junction Solar Cells .....	21
2.5 Definitions for the Characterization of Photovoltaic devices .....	23
3. METHODS AND RESULTS .....	26
3.1 Experimental Setup .....	26
3.1.1 Central Experiment .....	27

3.1.2	Pointing System .....	31
3.1.3	Auxiliary Sensors.....	32
3.1.4	Physical Layout .....	35
3.1.5	Control Software.....	36
3.2	Environmental Conditions during Experiments.....	39
3.3	General Considerations Used for Data Analysis.....	40
3.4	Results .....	42
3.4.1	Overview of Electrical Characteristics .....	42
3.4.2	Performance Under Varying Conditions .....	44
3.4.3	Performance of ATJ Solar Cells on Earth versus Space.....	56
4.	CONCLUSIONS .....	60
	BIBLIOGRAPHY .....	62
	A P P E N D I X E S .....	64
	Appendix A: Recombination Processes in Semiconductors .....	65
	Appendix B: Absorption in Direct Bandgap and Indirect Bandgap Materials .....	68

## LIST OF TABLES

Table 3.1: Main characteristics of the SCTU sensors connected to the general-purpose data logger .....	33
Table 3.2: Average temperature of solar cells under horizontal position testing .....	48
Table 3.3: Conversion Efficiencies and Fill Factors.....	51
Table 3.4: Electrical characteristics of ATJ solar cells operating in space compared to operation on earth .....	58

## LIST OF FIGURES

Figure 2.1: Position of Fermi level in a metal, insulator and semiconductor .....	3
Figure 2.2: Fermi-Dirac distribution function.....	5
Figure 2.3: Extra energy levels due to doping in a n-type semiconductor and in a p-type semiconductor. $E_{fn}$ and $E_{fp}$ are the new Fermi levels of the n-type and p-type semiconductors respectively due to doping .....	6
Figure 2.4: Junction in final equilibrium (isolated) .....	9
Figure 2.5: Energy diagrams, reverse (left) and forward bias (right) .....	13
Figure 2.6: Schematical cross-section diagram of a single-junction solar cell.....	15
Figure 2.7: Optimal bandgap for single junction solar cell [2].....	18
Figure 2.8: Lattice Constant and Bandgap Energy for Commonly Used Semiconductors [2] .....	20
Figure 2.9: Cross-sectional schematic diagram of the n/p InGaP/InGaAs/Ge ATJ cell.....	21
Figure 2.10: Typical external quantum efficiency for the ATJ cells .....	22
Figure 2.11: Typical I-V Curve.....	24
Figure 3.1: Block Diagram of the SCTU .....	26
Figure 3.2: Electrical circuit and temperature measuring system of the main experiment.....	28
Figure 3.3: ATJ solar cell set used in the SCTU (embedded thermocouples are shown).....	30
Figure 3.4: SCTU mobile platform pointing to the sun .....	32

Figure 3.5: Top-view mechanical layout diagram of SCTU mobile platform.....	35
Figure 3.6: Main components of the MASS/SCTU mounted in the field.....	35
Figure 3.7: Layout of components in the Primary and Secondary Electronics Enclosure.....	36
Figure 3.8: Flowchart of the general software operation .....	38
Figure 3.9: Solar Irradiance of the Day.....	40
Figure 3.10: I-V Curves of ATJ and Si solar cells.....	42
Figure 3.11: I-V curves along the day for the ATJ set (blue) and silicon set (red). Horizontal position. Maximum power points are marked by an asterisk (*)......	46
Figure 3.12: I-V curves along the day with temperature compensation (28°C) for the ATJ set (blue) and silicon set (red). Horizontal position. Maximum power points are marked by an asterisk (*) .....	47
Figure 3.13: I-V curves with sun tracking and temperature compensation for the ATJ set (left) and silicon set (right) .....	49
Figure 3.14: Conversion efficiencies during test day .....	51
Figure 3.15: Efficiency degradation with respect to the angle of incidence of the radiation for the ATJ solar cells.....	52
Figure 3.16 : Efficiencies of ATJ solar cells in horizontal and pointing to the sun positions along the day.....	53
Figure 3.17: Efficiencies along the day, with different temperature compensations, from 0° to 80° C.....	55
Figure 3.18: Conversion efficiency vs. temperature at maximum insolation instant. ....	56
Figure 3.19: I-V curve of ATJ solar cells operating in space under AM0 conditions (1353 W/m <sup>2</sup> ) at 28°C.....	57

Figure 3.20: I-V curve of ATJ solar cells operating on earth, with the solar cells pointing to the sun, compensated at 28°C .....	57
Figure 3.21: Solar spectra in space and on earth during experiments (Measured spectra was scaled for comparison purposes) .....	59
Figure A.1: Auger recombination with associated excess energy given to an electron in the conduction band: In the recombination process, the electron collides with another electron in the conduction band (1). After that, the second electron gains energy which is then dissipated as a phonons (2), no light is emitted.....	65
Figure A.2: Two step recombination process via a defect energy level, situated in the forbidden gap. The electron relaxes to an intermediate defect energy level (1), then recombines with a hole in the valence band (2).....	66
Figure A.3: Surface states lying within the forbidden bandgap at the surface of a semiconductor .....	67
Figure B.1: Schematical energy-momentum diagram for a direct bandgap material .....	68
Figure B.2: Schematical energy-momentum diagram for an indirect bandgap material .	69
Figure B.3: Energy-momentum diagram for silicon .....	70

## RESUMEN

Las celdas solares ATJ (Advanced Triple Junction) InGaP/InGaAs/Ge son uno de los dispositivos fotovoltaicos más eficientes disponibles en el mercado. En este trabajo se presenta su desempeño en la superficie terrestre, obteniéndose resultados notoriamente superiores a las tecnologías convencionales en todas las pruebas realizadas. Se determinan sus características eléctricas, parámetros de modelación relevantes (eficiencia y factor de llenado, dentro de otros) y se analiza el efecto de factores externos en su desempeño (ángulos de incidencia, efectos de la atmósfera y efectos de la temperatura).

El estudio realizado utiliza celdas solares ATJ comerciales las cuales a la fecha sólo están disponibles para aplicaciones satelitales. El análisis de los resultados obtenidos se realiza en comparación a la tecnología convencional de silicio, la cual fue sometida a pruebas equivalentes. Se demuestra que las características específicas para la operación en el espacio de las celdas ATJ en algo degradan su desempeño en la tierra, pero aún así se obtienen resultados ostensiblemente superiores respecto a la tecnología de silicio.

La metodología de análisis considera el desempeño de las celdas solares bajo condiciones atmosféricas cambiantes a lo largo de un día. Se captura información de voltaje, corriente y temperatura de las celdas, además de variables relevantes del entorno como el espectro solar incidente, la irradianza total y variables meteorológicas. Las celdas solares de prueba se instalan sobre una plataforma móvil capaz de orientarlas a posiciones arbitrarias incluyendo el seguimiento continuo del sol, permitiendo aislar el efecto coseno en la radiación incidente.

Este documento comienza con un análisis teórico para entender la tecnología convencional mono-capa y la tecnología multi-capas de las celdas ATJ. Posteriormente se muestran los métodos utilizados para la realización de los experimentos. A continuación, se analiza el desempeño de las celdas solares a lo largo del día considerando los distintos factores que la afectan. Finalmente, se compara el desempeño real obtenido en la tierra con los resultados en el espacio obtenidos por el fabricante.

## ABSTRACT

Advanced Triple Junction (ATJ) InGaP/InGaAs/Ge solar cells use state-of-the-art photovoltaic technologies which are based on multiple semiconductor junctions. This work analyzes their performance on the surface of the earth, obtaining noticeably-improved results compared to conventional technologies in all performed tests. The analysis takes into account the solar cells electrical characteristics, relevant modeling parameters (efficiency and fill factor, among others) and the effect of external factors affecting the performance (angles of incidence, effects of the atmosphere and temperature dependence).

This study uses commercial ATJ solar cells which are currently available only for satellite applications. Obtained results are compared to conventional silicon solar cells which are exposed to equivalent tests. It is demonstrated that specific space-construction characteristics of ATJ solar cells partially degrade their performance on earth, but anyway noticeably exceed the performance of the silicon technology.

The applied methodology considers the performance of the solar cells under varying atmospheric conditions along a day. Voltage, current and solar cell temperature are logged together with relevant environmental information such as the incident solar spectrum, total irradiance and weather variables. All solar cells are mounted on a mobile system capable of arbitrarily orienting their position (including sun-tracking), what allows to distinguish the cosine effect from the influence of the atmosphere in the incident radiation.

This document first presents a theoretical analysis to understand the single-junction (silicon) and multi-junction (ATJ) semiconductor technologies. After that, shows the applied methods to perform the solar cell characterization. Next, analyzes the performance of the solar cells along the day considering all factors that affect performance. Finally, compares the obtained results on earth to the results in space obtained by the manufacturer.

## 1 INTRODUCTION

Currently, more efficient photovoltaics devices are needed for the further development of market-competitive solar powered mobile devices, such as robots or automobiles. Today's standard technologies, such as silicon solar cells, have efficiencies that are not high enough to satisfy the high-power needs of mobile applications. Thus, more efficient technologies such as the ones used in space must be considered. This work analyzes the performance of Advanced Triple-Junction (ATJ) InGaP/InGaAs/Ge solar cells built for satellite use, when they are used on the surface of the earth.

This study is developed as part of the NASA-funded "Life in the Atacama" project, developed by Carnegie Mellon University with the collaboration of Pontificia Universidad Católica de Chile among other institutions. The Life in the Atacama project seeks to develop technology in support of robotic astrobiology for NASA while conducting useful Earth science in the Atacama Desert of northern Chile [Wett03]. Its purpose is to develop technology relevant to Mars in the form of an autonomous rover capable of traversing extremely long distances finding basic forms of life without direct human intervention. The final objective of this study is to characterize ATJ solar technology used in Zoe robot during field expeditions of years 2004 and 2005.

### 1.1 Objectives

This study determines the performance and electrical characteristics of ATJ solar cells operating under the influence of the ambient conditions on the surface of the earth. To achieve this, the performance of the ATJ solar cell is compared with that of traditional silicon solar cell designed for use on earth.

Experiments consist in exposing ATJ and silicon solar cells samples to normal outdoor ambient conditions, applying them several tests. They include an electrical characterization (current-voltage curve acquisition with a variable load), temperature measurements of the solar cells, and characterization of the environment (incident irradiance, incident spectra, and others). The solar cells and instruments are mounted on a mobile platform that can be oriented arbitrarily to quantify the

influence of the angle of incidence of the sunlight in the performance of the solar cell.

The data obtained from the tests is used to determine performance parameters such as conversion efficiencies, fill factors, temperature sensibilities and others. These choice of parameters are meant to simplify the comparison and characterization of the solar cells.

In order to understand the results in detail, this document presents a complete overview of basic concepts related to solar cell operation and specific ATJ solar cell concepts. Chapter 2 describes a general technical background including topics related to semiconductor basics, the photoelectric effect, construction characteristics of ATJ solar cells and technical definitions commonly-used for solar cell characterization. Finally, chapter 3 describes the methods used and the results obtained in this study.

## 2 TECHNICAL BACKGROUND

Before reviewing the technical characteristics of the Advanced-Triple-Junction (ATJ) solar cells, the basic operation of a single-junction cell will be discussed.

### 2.1 Semiconductor Basics

When discussing single atoms, electrons have their own discrete energy levels. In a solid state, however, these energy levels interfere with each other, resulting in energy bands, broader energy states that can be occupied by electrons. These energy bands are separated from each other by a zone with forbidden energy levels (bandgap). The energy band below the bandgap is called valence band, above the bandgap lies the conduction band. (See Figure 2.1).

At zero Kelvin, the electrons start to fill up the energy bands from the lowest level upwards, to a certain value, called the Fermi level. All energy bands above this level are empty. The position of this Fermi level and bandgap size determines whether a material is an electrical insulator, a semiconductor or a metal (electrical conductor).

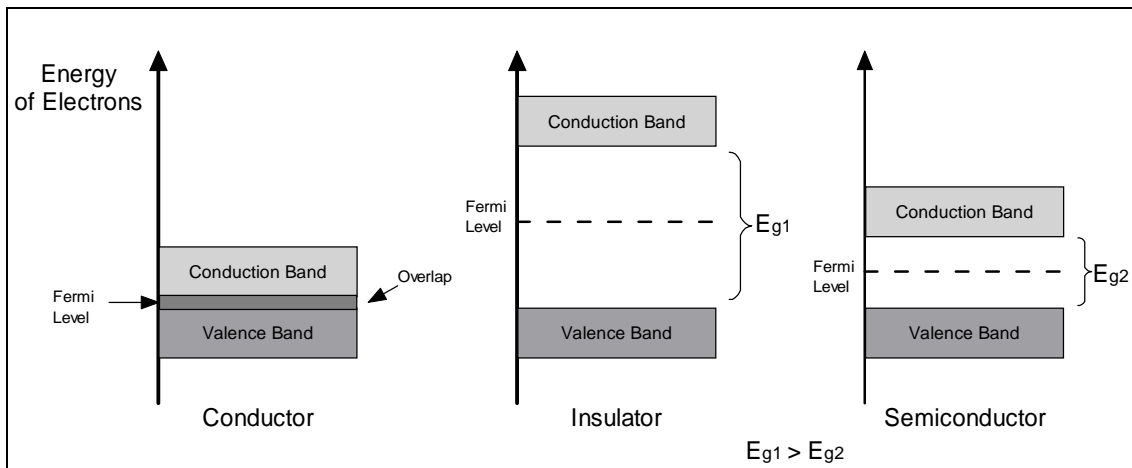


Figure 2.1: Position of Fermi level in a metal, insulator and semiconductor

From Figure 2.1, it follows that a metal is a very good electrical conductor, since the conduction band overlaps the valence band. Virtually no excess energy is needed to achieve electrical conductivity here, since electrons can freely move from one allowed level to another. In an insulator, however, the bandgap is very large, making it almost impossible to provide electrons with enough energy to make the transition to the conduction band<sup>1</sup>. On the other hand, in a semiconductor the Fermi level is also located in between both bands, but the bandgap is smaller, therefore the probability of electrons crossing the bandgap is higher. Additionally, crystalline semiconductors have a rigid/ordered nature arrangement of the molecular/atomic setup named the crystal lattice. The ordered lattice gives these materials properties similar to single atoms.

In solid states, at temperatures higher than absolute zero, electrons will occupy levels above the Fermi level (only in the allowed energy levels of the material). The distribution of electrons over the different energy levels is then given by the Fermi-Dirac formula, which represents the probability a certain energy level is occupied,

$$f(E) = \frac{1}{1 + e^{\frac{E-E_F}{k_B T}}}, \quad (2-1)$$

in this formula,  $k_B$  is the Boltzmann constant ( $1.38 \times 10^{-23} \text{ JK}^{-1}$ ), and  $T$  is the absolute temperature. The distribution is schematically drawn in Figure 2.2. At room temperature, some electrons will be in the conduction band, leaving an open position in the valence band. These positions are referred to as holes. In this situation, the material can conduct electricity, since electrons can freely move from one allowed

---

<sup>1</sup> The fact that the Fermi level in a semiconductor or insulator is located in the middle of its gap, does not mean there exists an electron population at that energy level. The population depends on the product of the Fermi function and the electron density of states. Therefore, in the gap there are no electrons since the density of states is zero. Also, at zero Kelvin, the conduction band is empty even though there are plenty of available states, but the Fermi function is zero, therefore, according to the Fermi-Dirac distribution no electrons will have that energy.

position to another allowed position in the conduction band (electron conduction). On the other hand, an electron in the valence band can move from its position to a vacant hole position, leaving a hole at its original position. It appears like the hole has moved in the opposite direction, a process called hole conduction.

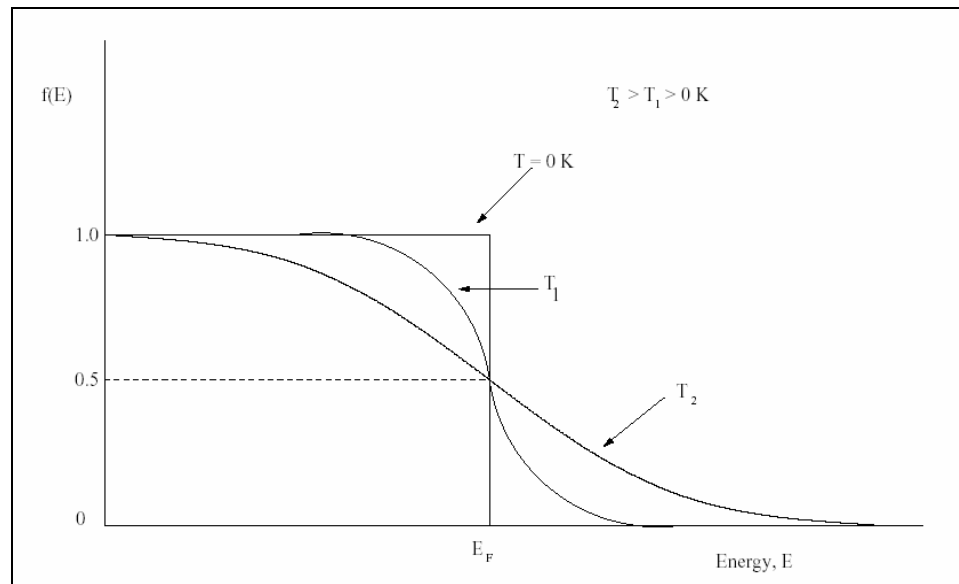


Figure 2.2: Fermi-Dirac distribution function

### 2.1.1 Semiconductor Doping

Yet another method for improving the electrical conductivity of a semiconductor by orders of magnitude is known as doping. In a pure semiconductor material like silicon, the atoms are all ordered in a specific lattice, forming covalent bonds with the neighboring atoms. Since silicon has four electrons in its outer shell, four covalent bonds are formed. Minor electrical conduction occurs when such a covalent bond is broken. The electron that is freed can move through the solid, the hole that is left behind can move due to hole conduction. The doping process, in which the pure material is ‘contaminated’ with strange atoms, can enlarge this electrical conductivity by orders of magnitude. Two types of doping can be distinguished: n-type and p-type doping. In n-type doping, a pure semiconductor,

like silicon, is mixed with tiny amounts of an element that has one extra electron in the outer shell (donor atoms). An example of such an element is phosphorus (P). The phosphorus atoms are incorporated in the specific silicon lattice by replacing Si atoms (substitutional). As a result, four of the five electrons in the outer shell of phosphorous form a covalent bond with electrons from the silicon atoms. The fifth electron is very loosely bound and can be freed quite easily. n-Type silicon is electrically neutral, since the pure silicon is mixed with electrically neutral phosphorus atoms. However, the electrical conductivity has greatly improved, due to the doping process. In p-type doping, a pure semiconductor material like silicon is 'contaminated' with an element with only three electrons in its outer shell (acceptor atoms), for example boron (B). The three electrons form a covalent bond with the outer electrons of the silicon atoms, leaving a hole at the place where a fourth electron would fit in. The hole conduction mechanism can provide electrical conductivity in this situation. Just as n-type material, p-type material is electrically neutral.

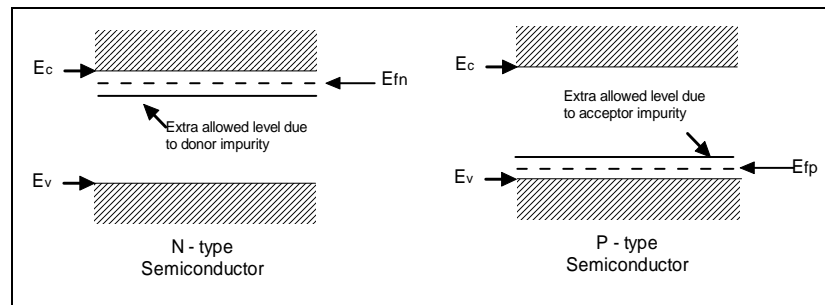


Figure 2.3: Extra energy levels due to doping in a n-type semiconductor and in a p-type semiconductor.  $E_{fn}$  and  $E_{fp}$  are the new Fermi levels of the n-type and p-type semiconductors respectively due to doping

The addition of n-type or p-type impurities to a pure semiconductor like silicon, allows new energy levels in the bandgap. The extra energy level due to n-

type doping, is situated just below the conduction band. This occurs since the fifth electron is very loosely bound and little energy is needed to promote the electron to the conduction band. In an analogous way, the extra energy level due to p-type doping, is situated just above the valence band, so that very little energy is required to achieve hole conduction (see Figure 2.3). Also, the Fermi level of the n-type material is now situated in between the new extra level and the conduction band in the bandgap. Analogously, in the p-type semiconductor, the Fermi level is located below the new extra energy level and over the valence band (see Figure 2.3).

At room temperature, there is some thermal energy available to the electrons in the lattice due to vibrations. If an electron absorbs some of this energy, it may be promoted to a higher energy level (e.g. from the valence band to the conduction band). In n-type materials two different "kinds" of electrons are present (called majority carriers): those that begin at the donor level, and those that begin in the valence band. There are far more electrons in the valence band than at the donor levels. However, the energy needed by the valence electrons to traverse from the band gap to the conduction band is far greater than the energy needed by the electrons at the donor level to get to the conduction band.

In n-type materials, when donor level electrons are thermally promoted to the conduction band, a donor level is left empty. These electrons are called majority carriers (for n-type materials)  $n_M$ , and is given by the Boltzmann statistics approximation<sup>2</sup> (in this estimate, electrons promoted from the valence band are neglected, since their number is insignificant in comparison to the number of electrons from the donor level ),

---

<sup>2</sup> The Boltzmann statistics, is given by:  $\frac{n_1}{n_2} = e^{\frac{-(E_2-E_1)}{kT}}$ , and approximates the

concentration of carriers at some energy level  $E$ , where  $n_1$  and  $n_2$  are the concentration of carriers at potential energies  $E_1$  and  $E_2$ . This approximation can be used since the concentration of electrons in the conduction band is never large enough to consider the Pauli exclusion principle important. In this work the concentration of carriers is addressed as number of carriers for simplicity.

$$n_M = A_M e^{\frac{(E_{cn} - E_{fn})}{kT}}, \quad (2-2)$$

where  $E_{cn}$  is the energy at the bottom of the conduction band in the n-type material,  $E_{fn}$  is the Fermi level in the n-type material, and  $A_m$  is the number of n-type dopant atoms.

Conversely, the number of valance electrons promoted to the conduction band is small. Note that when a majority carrier is promoted from a donor level, the lattice itself is unaffected. However, when a valance electron is promoted, it leaves a hole behind in the lattice. The hole is called a minority carrier. The number of minority carriers,  $n_m$ , is given by the Boltzmann statistics,

$$n_m = A_m e^{\frac{E_{fn}}{kT}}, \quad (2-3)$$

where  $A_m$  is the number of atoms in the lattice.

In p-type materials, electrons from the valance band are being promoted either to the conduction band or to the acceptor levels, leaving conducting holes behind in the valance band. To determine the number of holes, the number of electrons that were promoted to create the holes must be obtained. In p-type materials, the number of majority carriers, or holes created by electrons getting promoted to the acceptor levels, is  $h_M$ , and is given by,

$$h_M = A_M e^{\frac{E_{fp}}{kT}}, \quad (2-4)$$

where  $E_{fp}$  is the Fermi level in the p-type material, and  $A_M$  is the number of p-type acceptor atoms in the lattice. When an electron is promoted from the valance band all the way to the conduction band, it leaves behind a conducting hole which becomes a conducting agent itself. Electrons in the conduction band of p-type material are called minority carriers, and their number,  $h_m$  is given by,

$$h_m = A_m e^{\frac{(E_{cp} - E_{fp})}{kT}}, \quad (2-5)$$

where  $A_m$  is the number of atoms in the lattice and  $E_{cp}$  is the energy at the bottom of the conduction band in the p-type material.

### 2.1.2 P-N Junction Operation

In a p-n junction, p-type material is in contact with n-type material in the same integral crystal. The Fermi level of the p-type material is much lower than that of the n-type material with respect to the top of the valance band in the n-type material (see Figure 2.3). Therefore, when the two are juxtaposed in an integral substance, the Fermi levels must equilibrate. This equilibration occurs because the electrons residing in the donor levels of the n-type material are exposed to lower energy levels. Electrons always seek the lowest energy level, so they begin to diffuse over to fill the acceptor and valance levels in the p-type material, where the density of electrons is lesser (analogously, holes seek higher energy levels, therefore the opposite occurs).

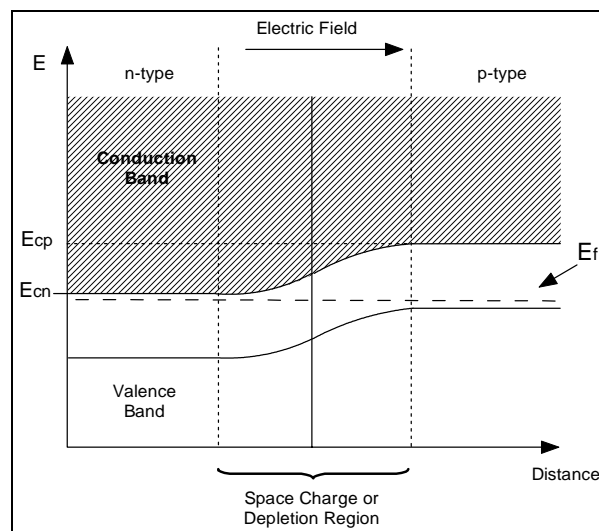


Figure 2.4: Junction in final equilibrium (isolated)

Fermi levels begin to move closer to each other until finally, they meet in the middle (see Figure 2.4). At this point, the contact potential difference between the two material types is just enough to prevent further diffusion of electrons and holes across the junction. When the Fermi levels have equilibrated, there are no longer lower energy levels in the vicinity for n-type electrons to occupy, so they stop migrating, and the system is again in equilibrium.

There is now only one Fermi level ( $E_f$ ) and the whole crystal has undergone through what is known as band bending. The Fermi level was equilibrated, and all of the rest of the bands in each type of the semiconductor moved relative to it. The depletion region is the region in the crystal in which the bands are bent. As shown in Figure 2.4, the bottom of the conduction band in the p-type material is now higher than the bottom of the conduction band in the n type material. This potential difference between energy levels in the depletion region grows until it is just large enough to oppose further movement of majority carriers. The contact potential is what displaces the p-type and n-type bands, and its electric field points in the direction that a positive charge would be inclined to move.

### **2.1.3 Isolated P-N Junction**

In an isolated p-n junction, the majority carriers on the n-type side (electrons) will not move toward the p-type side, because in order to do so, they would have to move up to a higher energy level. The minority carriers (holes) on the n-type side, on the other hand, will move easily to the p-type side, since holes seek higher energy levels. On the p-type side, the majority carriers are holes. They will be deterred from crossing the depletion region, since at the other side the energy levels would be lower. Conversely, the minority carriers in the p-type side (electrons) easily move down to the n-type, since there the energy levels are lower. As a final result, the vast majority of mobile carriers are not able to cross the junction.

The thermally generated minority carriers can easily flow across the junction, creating what will be referred as the thermal current ( $I_t$ ). The thermal current from the p-type side is proportional to the number of electrons thermally promoted to the conduction band. Therefore, from Equation 2-5,

$$I_m = Ce^{\frac{(E_{cp}-E_f)}{kT}}, \quad (2-6)$$

where C is an experimentally determined constant of proportionality related to the dopant concentration.

In the n-type material, the thermal current is from holes moving across the junction, so the n-type contribution to thermal current is proportional to the number of hole minority carriers in the n-type material which comes from Equation 2-3. Then,

$$I_m = Be^{\frac{E_f}{kT}}. \quad (2-7)$$

The total thermal current is also called the reverse saturation current, or the dark current. Note that because  $I_p$  is due to electrons flowing from the p-type material to the n-type material and  $I_m$  is due to holes flowing from the n-type material to the p-type material, they are additive (have same sign). Then total thermal current,  $I_T$ , is the sum of the two.

In an electrically isolated situation, there can be no net current through the junction. Thus, there must be another component of current that opposes the thermal current. This component is called the recombination current, and is comprised of majority carriers traversing the p-n junction in the "wrong" direction. Only majority carriers that have been thermally promoted to a high enough energy level, such that the energy level of the other side "looks" desirable, will cross the junction. More specifically, an electron on the n-type side of the material (majority carrier), would merely move to the p-type side if it could gain a lower potential by doing so. This means, it would have to be in an energy level in the n-type conduction band with a higher potential than the top of the conduction band in the p-type material ( $>E_{cp}$ ). The opposite occurs with the majority carriers (holes) in the p-type side.

Quantitatively, the recombination current is proportional to the number of majority carriers that can cross the junction. In the n-type material, the

contribution to the recombination current is proportional to the number of electrons that can cross to the p-type side of the junction,

$$I_m = Ce^{\frac{(E_{cp}-E_f)}{kT}}, \quad (2-8)$$

where C is the same than in equation 2-6. Analogously, the contribution to the recombination current due to holes crossing the junction to the n-type side of the material is proportional to the number of holes that are created in the p-type side at energies below the top of the n-type valance band. This contribution is

$$I_m = Be^{\frac{E_f}{kT}}, \quad (2-9)$$

where B is the same than in equation 2-7. The Boltzmann statistics considers here the energy difference between  $E_{cn}=0$  and the acceptor levels. Note that the thermal current from the p-type side (Equation 2-6) is equal to the recombination current from the n-type side (Equation 2-8), and the thermal current from the n-type side (Equation 2-7) is equal to the recombination current from the p-type side (Equation 2-9). This ensures that the total junction current will be zero (the constants B and C are also equal if the p-type and n-type dopants have been added in equal proportions). It is useful to note that while thermal current depends only on temperature, total recombination current depends on temperature and on the external voltage (forward or reverse bias, see next section).

### 2.1.3 Forward and Reverse Bias

To make the junction reversed biased, the positive lead of a battery is connected to the n-type side and to ground (potential=0) and the negative lead to the p-type side (see Figure 2.5, “Reverse Bias”). In this case, the potential on the n-type side remains constant at zero, but the potential of all the energy levels on the p-type side are raised by an amount  $eV$ , where  $e$  is the charge of the electron and  $V$  is the value of the applied potential. Therefore, the energy hill becomes even steeper, and it becomes even less likely for majority carriers to cross the junction (note that the Fermi level is still continuous, but is bent by the applied potential). The net junction current is no longer zero, since the thermal current remains essentially constant, but

the recombination current shrinks proportionally to the increase in potential difference.

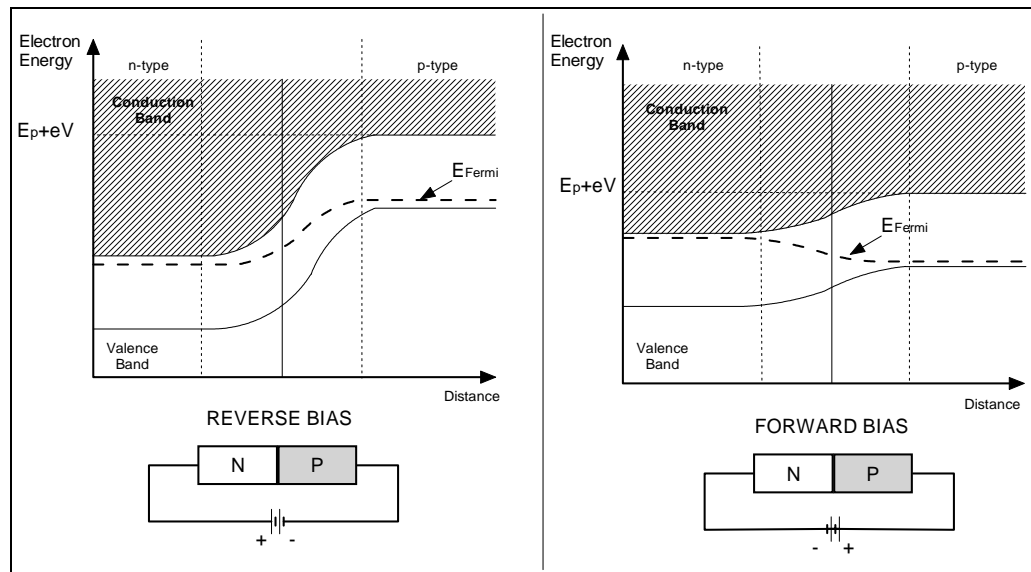


Figure 2.5: Energy diagrams, reverse (left) and forward bias (right)

If the junction instead is forward biased, by attaching the negative end of the battery to the n-type side and ground, and the positive battery lead to the p-type side (see Figure 2.5 “Forward Bias”), the opposite occurs. Every energy level on the p-type side is reduced by an amount  $eV$ , making it more probable that majority carriers will cross the junction. In fact, if the potential applied is great enough, the potential hill will become flat or even reverse its direction, making it energetically favorable for majority carriers to cross the junction. In this case, the semiconductor will conduct electricity. In a forward biased situation, the thermal current remains constant, but the recombination current grows in proportion to the applied potential. The new recombination current has two parts; one is from the n-type side, and is given by,

$$I_{mfb} = Ae^{\frac{(E_{cp} - E_{fn} - eV)}{kT}}. \quad (2-10)$$

The contribution to the current from the p-type side will be,

$$I_{rpfb} = Me^{\frac{(E_{fp} - eV)}{kT}}, \quad (2-11)$$

which is bigger than the recombination current from the p-type side in the unbiased junction (Equation 2-9). Upon inspection, it can be found that the total forward biased recombination current is just the unbiased recombination current multiplied by the Boltzmann factor ( $e^{\frac{\Delta E}{kT}}$ ), with  $\Delta E = eV$  resulting,

$$I_{Rfb} = I_R e^{\frac{eV}{kT}}, \quad (2-12)$$

where here,  $I_R$  is the total recombination current in the isolated cell, and is equal to the total thermal current  $I_T$ . From here, the total net electron current through the forward biased junction may be found. If we consider a cell that has been carefully doped so that the constant coefficients of the current terms are equal, we can calculate the total current in a forward biased junction. The total junction current must be the thermal current plus the recombination current,

$$I_j = I_{Rfb} + I_T. \quad (2-13)$$

When the coefficients are equal,  $I_{Rfb}$  can be written in terms of  $I_T$ , as mentioned above, so that, finally, the total junction current in a forward biased junction is simply,

$$I_j = I_T \left( e^{\frac{eV}{kT}} - 1 \right). \quad (2-14)$$

## 2.2 Photovoltaic Cell Operation

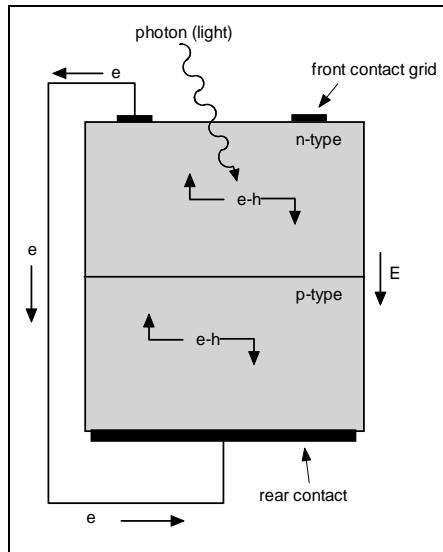


Figure 2.6: Schematical cross-section diagram of a single-junction solar cell

A single-junction photocell is just a p-n junction with metallic rear and front contacts that allow electron conduction to an external load. The front contacts cover only partially the semiconductor to allow the light to enter. In Figure 2.6 a schematical cross-section diagram of a single-junction solar cell is displayed.

In order to promote an electron into the conduction band, an incoming photon must have energy at least equal to the band gap (assuming all the electrons in the donor levels have already been thermally promoted). Therefore, photons of wavelength less than  $hc/E_g$  ( $h$  is the Planck constant,  $c$  the speed of light, and  $E_g$  the bandgap energy) will make no contributions to generate electricity in the cell. However, photons with sufficient energy will promote electrons with a certain efficiency rate (see Recombination Processes in Semiconductors appendix in pg. 65) and they will, in the presence of an external load, produce a current through the cell. This current is called the photocurrent, and is given by,

$$I_p = \frac{eF\tau}{T_r}, \quad (2-15)$$

where  $e$  is the charge of the electron,  $F$  the total number of carriers produced each second by absorbed photons (the efficiency is implicit in  $F$ ),  $\tau$  is the effective lifetime of the carriers, and  $T_r$  is the transit time, or the time spent by the carriers in moving to the electrode of the cell.  $T_r$  is a quantity that groups several terms,

$$T_r = \frac{L^2}{\mu V}, \quad (2-16)$$

where  $L$  is the electrode spacing,  $\mu$  is the drift mobility (another quantity that has to do with efficiency) and  $V$  is the applied voltage.

### 2.2.1 Separation of Charge

When photons enter the semiconductor to which no external voltage has been applied (see Figure 2.4 and Figure 2.5), they add a form of energy in addition to heat. The photons interact with atoms in the lattice, in general, a single photon collides with a single electron, imparting its energy to the electron. When  $h\nu > E_g$  ( $h\nu$  is the photon energy, where  $\nu$  is its frequency), the electron is promoted to a higher energy level if the electrons have the right momentum (See Absorption in Direct and Indirect Bandgap Materials appendix in pg. 68). On the n-type side, they promote electrons into the conduction band, leaving holes in the valence band that can see the junction field and be swept across to the p-type side. Once they reach the p-type side, however, they cannot re-cross the junction; to do so would be to oppose the field. In the p-type material, electrons become promoted to the conduction band and roll easily down the “hill” into the n-type side, but once they are there, they cannot re-climb the hill. This is analogous to an increase of the thermal current. Separation of charge begins to build up, because an excess of electrons become trapped on the n-type side while an excess of holes are trapped on the p-type side. This separation of charge competes with and eventually overcomes the junction field and forms a forward biased junction.

### 2.2.2 Isolated Photocell

If the junction is electrically isolated, the forward bias will not last. Also the net current must be zero, so the recombination current must somehow compensate. The sum of the total junction current (Equation 2-14) and the newly created photocurrent must be zero, so that,

$$I_j = |I_p| = I_T \left( e^{\frac{eV_{oc}}{kT}} - 1 \right), \quad (2-17)$$

where  $I_p$  flows from the n-type side to the p-type side, while  $I_j$  flows from the p-type material to the n-type material. In the above equation, the applied potential  $V_{oc}$  is the potential difference set up by the photocurrent. It is the voltage created by the photons, and it is called the open circuit voltage. Physically, the majority carriers cross the junction until a situation has been reached in which the difference in potential between the p-type side and the n-type side has "unbent" the bands exactly. In such a situation, there is no preferred direction for carriers to go, and the system reaches an equilibrium. Then the open circuit voltage must be exactly equal to the contact potential in the junction. Experimentally, this is exactly the case. The open circuit voltage of silicon photovoltaic cells is between 0.5 V and 0.7 V, which is the range of "turn-on potential" in silicon diodes. From this realization, the current equation (2-14) can be solved to find the open circuit voltage, which gives,

$$V_{oc} = \frac{kT}{e} \left( \ln \left( \frac{I_p}{I_T} + 1 \right) \right). \quad (2-18)$$

### 2.2.3 Photocell with Load

If the cell is connected to an electric circuit with some load a net current will flow through the junction. It is more energetically favorable for the charge build-up to dissipate through a load than for the recombination current to increase by as much as it is necessary for the junction current to match the photocurrent. Therefore, when connected to a load, the photocurrent will in fact discharge across it, creating useful electrical energy. The current through the load will be,

$$I_L = I_p - I_j. \quad (2-19)$$

We can again solve this equation for  $V$  to find the potential drop across the cell, or the effective "battery voltage" created by the photocell,

$$V_e = \frac{kT}{e} \ln \left( \frac{I_p - I_L}{I_T} + 1 \right). \quad [\text{Angr92}] (2-20)$$

### 2.3 Design Considerations

Design restrictions include selecting an optimal energy bandgap of the semiconductor. This yields in a tradeoff between absorbing a small number of high-energy photons versus absorbing a wider spectra of photons with higher thermal losses. Figure 2.7 shows maximum allowable efficiencies for different bandgap energies and corresponding well-known semiconductors used in solar cells.

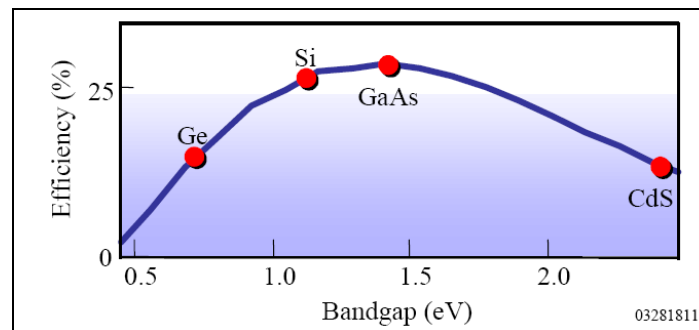


Figure 2.7: Optimal bandgap for single junction solar cell [Nrel00]

Relevant electrical parameters of a solar cell depend both on the number of freed electrons and on their energy. Voltage levels are proportional to the bandgap energy difference; current levels are proportional to the number of electrons freed to the conduction band. Therefore, choosing an energy bandgap implies a tradeoff between high voltages (high energy bandgaps) or high currents (low energy bandgaps).

## 2.4 Multi-Junction Solar Cells

Multi-junction solar cells use multiple semiconductor junctions, each with different bandgap energies to minimize losses of low-energy photons and excess energy of energetic photons. Each individual semiconductor absorbs photons at specific wavelengths, with the resulting solar cell absorbing a broader spectrum with higher efficiencies due to reduced thermal losses.

Physically, the different semiconductors are stacked together ordered according to their bandgap energies. Incident photons first strike materials with the largest bandgap, absorbing the more energetic photons. Lower-energy photons travel across the semiconductor and are absorbed in successive layers with lower bandgap energies. If the bandgap of the semiconductor is larger than the energy of the photon, the material will be transparent.

### 2.4.1 Construction Procedure

There are two major approaches to the construction of multi-junction solar cells. The mechanically stacked approach physically stacks independently-grown layers. This system finds its main applications in optical concentrator systems. But the bulkiness, additional expense, and heat-sinking challenges make these multi-junction cells a less-desirable alternative [Nre100]. The second approach is the monolithically grown, where each semiconductor is sequentially grown on top of the other as one single piece. Monolithically-grown solar cells and their design restrictions will be analyzed with further details due to its importance for understanding ATJ solar cells.

Monolithically-grown multi-junction solar cells are expected to work at higher voltages and lower currents than a single-junction solar cell. The presence of specific semiconductor junctions for specific bands of the spectra yields in that each material individually absorbs fewer photons (e.g. a narrow band of the spectra), therefore generating lower currents. On the other hand, the series architecture and the absorption of more energetic electrons in several stages yields to higher voltages.

All semiconductors used in monolithically grown solar cells must have a similar crystal structure (e.g. lattice constant<sup>3</sup>) in order to produce optical transparency and maximum current conductivity between the top and bottom cells. A mismatch in the crystal lattice may produce mechanical defects and potentially constitute a source for electron-hole recombinations (see appendix A, Recombination Processes in Semiconductors, pg. 65). Figure 2.8 shows commonly-used semiconductors in solar cells (III-V materials). Semiconductors with different bandgaps and similar lattice constants are desired.

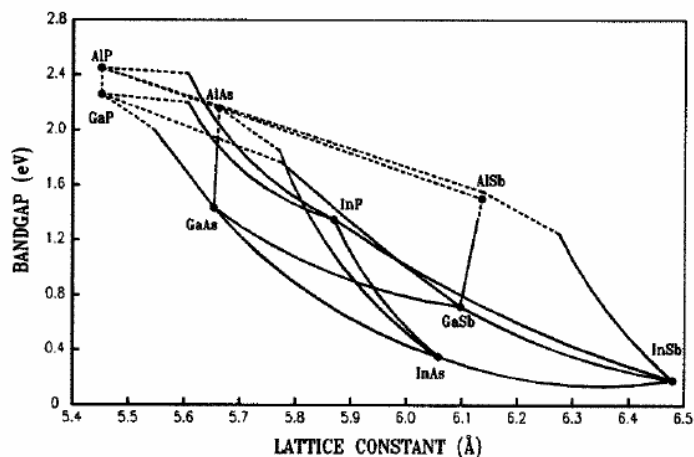


Figure 2.8: Lattice Constant and Bandgap Energy for Commonly Used Semiconductors [Nrel00]

Additionally, the serial architecture of monolithically-grown solar cells makes matching of currents a desirable characteristic. This is due to the total current limitation imposed by the layer with the smallest current contribution.

---

<sup>3</sup> Lattice constant is a measure of the distance between base atoms locations in a crystal pattern and has a strong descriptive correlation with the overall crystal structure [Nrel00].

The main difficulty in monolithic solar cells is the transportation of electrons between layers. The problem is addressed using a tunnel junction, which is a stack of highly-doped layers, which produce an effective potential barrier for both minority-carriers. The strong doping is necessary in order to have a thin depletion region, promoting tunneling across the junction and minimizing optical losses (photon absorption in the tunnel junction).

#### 2.4.2 Advanced Triple Junction Solar Cells

Advanced Triple Junction (ATJ) Solar Cells are high-efficiency multi-junction PV devices manufactured by Emcore Photovoltaics for space applications. Each unit is comprised of several semiconductor layers, which are monolithically grown over Ge wafers. The solar cell has three main junctions that individually take advantage of a different section of the incident radiation spectrum. Figure 2.9 [Stan00] displays a cross-sectional schematic diagram of an ATJ solar cell, with its three junctions.

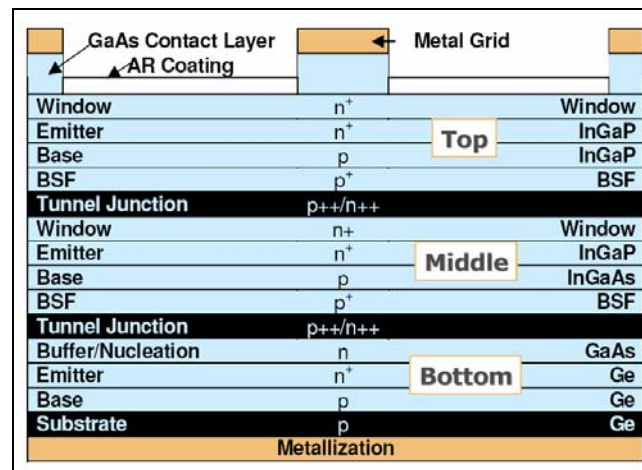


Figure 2.9: Cross-sectional schematic diagram of the n/p InGaP/InGaAs/Ge ATJ cell

The first junction, which takes advantage of the UV light, is built from InGaP, and has the largest bandgap of three junctions. The medium junction is

constructed of InGaP/InGaAs, and has medium sized bandgap, which makes the most of the visible light. Finally the bottom layer is constituted of germanium, which receives all the photons not absorbed by the other layers, and consequently has the smallest bandgap. The plot in Figure 2.10 [Stan00] shows the quantum efficiency of the ATJ cells, with each curve representing a junction.

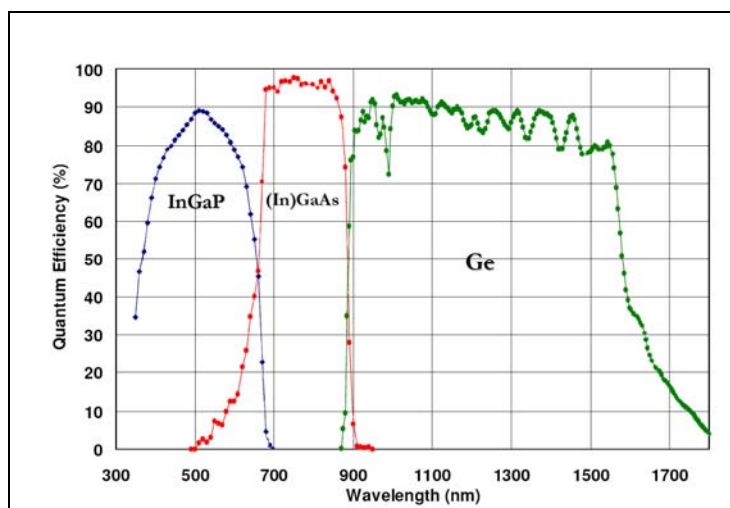


Figure 2.10: Typical external quantum efficiency for the ATJ cells

ATJ solar cells include several features that allows them to generate electricity with high conversion efficiencies. Among them, the use of window and back surface field (BSF) layers, which are high-bandgap layers that reduce recombination effects due to surface defects, shifting the electron-hole pair generation to places nearer the junction. Additionally, the InGaP top and InGaAs middle cells are lattice matched to the Ge substrate, therefore defects between layers are minimized.

The n- and p- contact metallization is mostly comprised of Ag, with a thin Au layer to prevent oxidation. The antireflection coating (AR) is a broadband dual-layer  $\text{TiO}_x/\text{Al}_2\text{O}_3$  dielectric stack, whose spectral reflectivity characteristics are designed to minimize reflection in broad band of wavelengths.

The InGaP/InGaAs/Ge advanced triple-junction (ATJ) solar cells are epitaxially grown in organo-metallic chemical vapor deposition (OMCVD) reactors on 140- $\mu\text{m}$  uniformly thick germanium substrates.

The solar cell structures are grown on 100-mm diameter (4 inch) Ge substrates with an average mass density of approximately 86 mg/cm<sup>2</sup>. Each wafer typically yields two large-area solar cells. The cell areas that are processed for production typically range from 26.6 to 32.4 cm<sup>2</sup>. The epi-wafers are processed into complete devices through automated robotic photolithography, metallization, chemical cleaning and etching, antireflection (AR) coating, dicing, and testing processes.

## 2.5 Definitions for the Characterization of Photovoltaic devices

The following photovoltaic definitions are extensively used in this document. These are basic concepts required to understand and characterize the performance of solar cells.

### a) Current-Voltage (I-V) Curves

Solar cells can be operated over a wide range of voltages and currents. I-V curves are used to measure the electrical characteristics of photovoltaic (PV) devices, and are normally presented as “current-voltage characteristic curves”, or “I-V curves”. These curves are obtained by varying continually the load resistance from open-circuit to short-circuit states, registering the voltage and current values. During this measurements, the PV devices are exposed to a constant level of light and the temperatures of the solar cells are kept constant. I-V curves graphically display typical relevant electrical parameters required for solar cell characterization. Figure 2.11 displays a typical I-V curve plot.

On an I-V plot, the ordinate refers to current, and the abscissa to voltage. The I-V curve passes through two significant points, the *short-circuit current* ( $I_{sc}$ ) and the *open-circuit voltage* ( $V_{oc}$ ). The  $I_{sc}$  refers to the current when the output terminals of the cell are short-circuited. In the plot this point is the intercept of the

curve with vertical axis. The  $V_{oc}$  is the voltage measured at open circuit conditions and is represented as the intercept of the curve with the horizontal axis in the plot.

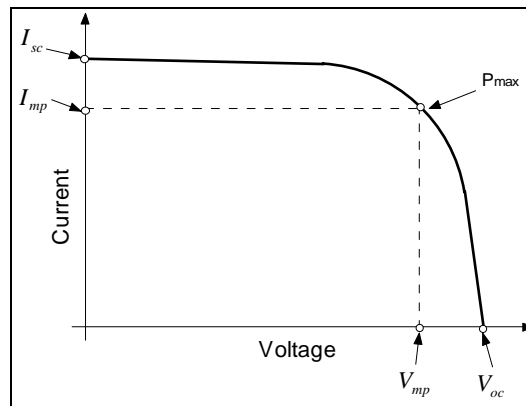


Figure 2.11: Typical I-V Curve

b) Maximum Power ( $P_{mp}$ )

The solar cell may be operated over a wide range of voltages and currents by varying the load resistance from zero to infinity. The Maximum Power ( $P_{mp}$ ) point occurs when the product of the current and voltage is maximum. The current and voltage at the maximum power point are denoted by  $I_{mp}$  and  $V_{mp}$ , respectively. (See Figure 2.11).

c) Fill Factor (FF)

The fill factor (FF) percentage measures the "squareness" of the I-V curve. It states the degree to which the voltage at the maximum power point ( $V_{mp}$ ) matches the open-circuit voltage ( $V_{oc}$ ) and that the current at the maximum power point ( $I_{mp}$ ) matches the short-circuit current ( $I_{sc}$ ). Therefore, a more "squared" I-V curve will have a higher fill factor. This relation is given by.

$$\text{Fill Factor (FF)} = \frac{I_{mp} \cdot V_{mp}}{I_{sc} \cdot V_{oc}} [\%] \quad (2-21)$$

d) Conversion Efficiency ( $\eta$  %)

The conversion efficiency of a solar cell is the percentage of the total incident solar energy on a photovoltaic device that is converted into electrical energy. This relation is given by

$$\text{Conversion Efficiency} = \frac{P_{mp}}{\text{Incident Solar Energy}} [\%] \quad (2-22)$$

e) Quantum Efficiency (QE)

Quantum efficiency (QE) is the ratio of the number of charge carriers collected by the solar cell to the number of photons of a given energy incident on the PV device. QE therefore is related to the response of a solar cell to the various wavelengths in the spectrum of incident light on the cell. The QE is given as a function of either wavelength or energy.

### 3. METHODS AND RESULTS

#### 3.1 Experimental Setup

All experiments carried out in this work are performed using the Solar Cell Testing Unit (SCTU). The SCTU is a sophisticated custom-made testing system able to thoroughly characterize the performance of solar cells in real outdoor conditions. The SCTU is assisted by a Multipurpose Autonomous Solar Station (MASS), which provides the SCTU with power, hardware and software to capture, filter and display the results, among other secondary capabilities. The MASS allows the SCTU to be operated for long periods of time in isolated places without direct human intervention.

The most relevant component of the MASS used by the SCTU is a main computer which provides processing power, storage and IO capabilities. The computer additionally incorporates several interfaces including RS/232 ports, USB and an analog/digital IO board.

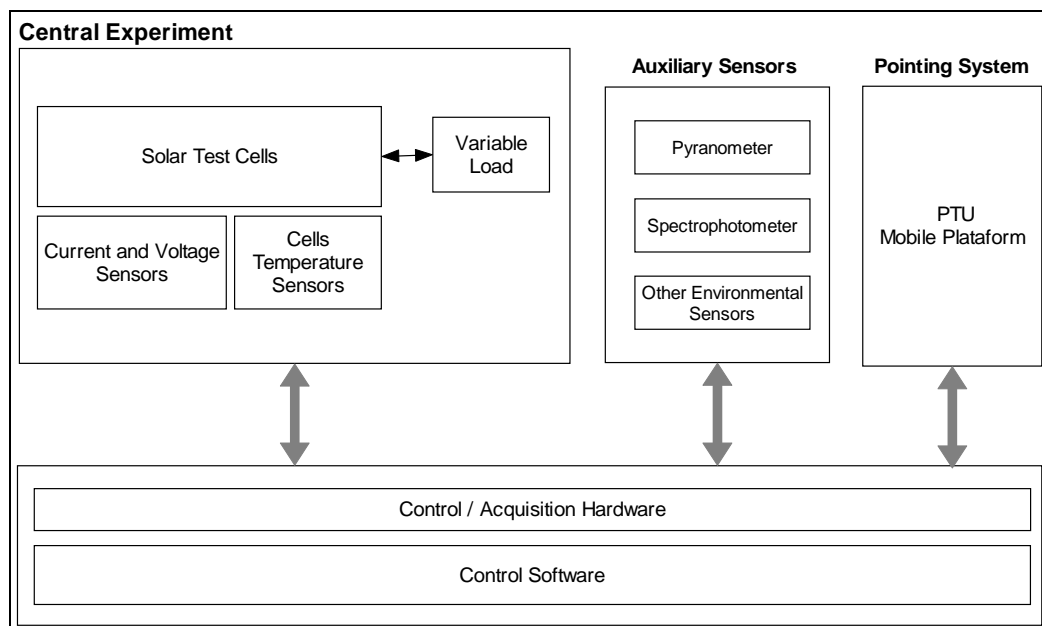


Figure 3.1: Block Diagram of the SCTU

The SCTU is comprised of three main modules that provide complementary data for solar cell characterization, as described in Figure 3.1. The “central experiment” performs direct tests to the solar cells, including an electrical characterization and solar cell temperature measurement; the “auxiliary sensors” provide with complementary environmental data that affect the performance of these devices; and the PTU (pan/tilt unit) allows to change the incident position of the solar cells. The complete experiment is coordinated by the control software / hardware which reside in the MASS.

### **3.1.1 Central Experiment**

As recently discussed, the central experiment performs direct tests on the solar cells including electrical characterization and solar cell temperature measurements. The electrical characterization determines current-voltage (I-V) curves of the solar cells. These curves are characteristic to the specific solar cell technology used.

The SCTU allows to test two independent sets of solar cells which are analyzed on a consecutive basis. The same load and current/voltage sensors are switched to the appropriate solar cell set when performing tests. Therefore comparative results are obtained because both experiments are performed under equivalent conditions.

The SCTU tests a set of Siemens “Standard 103mmx103mm Type 2” mono-crystalline silicon solar cells (conventional technology) and a set of the newly commercially-available Emcore “Advanced Triple Junction (ATJ) n/p InGaP / InGaAs / Ge solar cells”, traditionally used on satellites. The implemented electric circuit is shown in Figure 3.2. The figure shows the serial configuration of interconnecting cells, together with the output connectors for the solar panel.

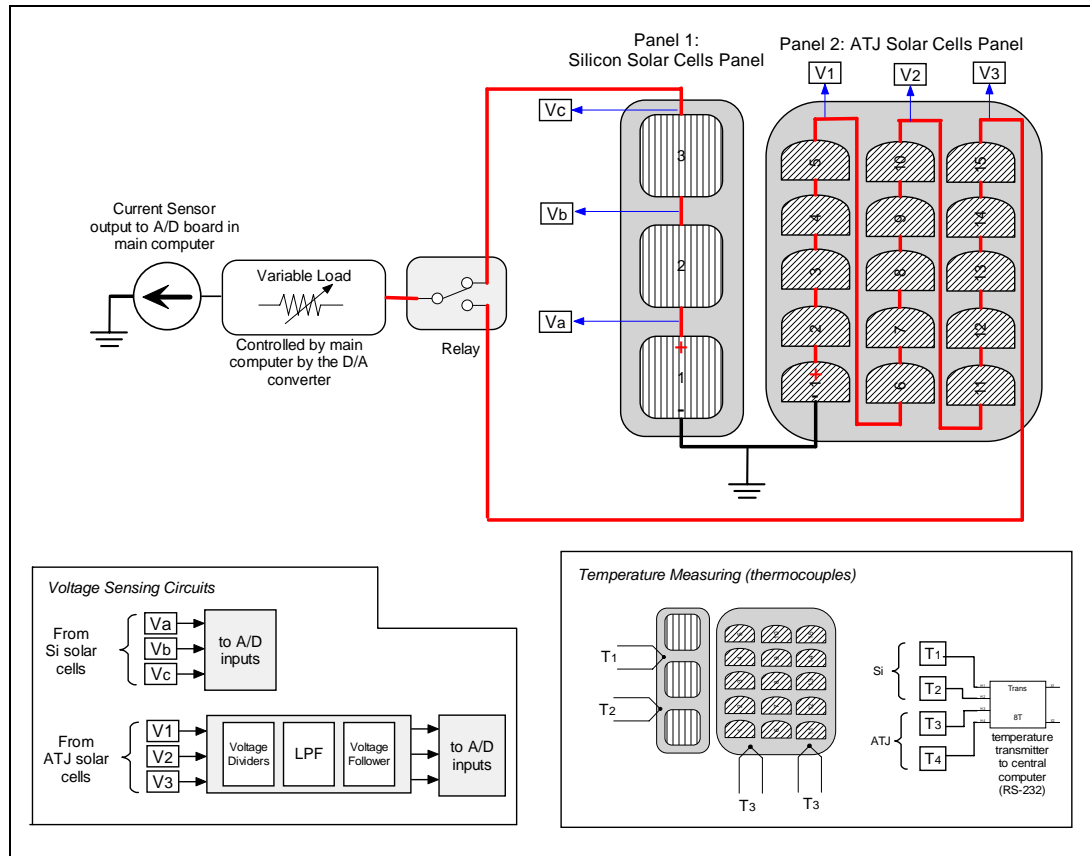


Figure 3.2: Electrical circuit and temperature measuring system of the main experiment

#### a) Load control

A single electronically-controlled load (Executive Engineering EE30180A DC) is connected to the set of solar cells to be tested. The device acts as a current regulator, forcing the current to be proportional to a voltage signal controlled by the D/A converter of the main computer. If the solar panels cannot deliver the demanded current, the load acts as short-circuit. The control software must be appropriately designed so that the variable load covers the complete range of operation of the specific solar cells used, including sufficient points to generate high-resolution and complete I-V curves (open-circuit to short-circuit).

The SCTU uses a Potter & Brumfield KUP-14D15-12 3PDT switching relay to connect each solar panel to the variable load (using a single contact). This relay is indirectly controlled by a digital output from the main computer through a solid-state opto-relay.

#### b) Current Measurement

Current measurements of the solar cells are performed using a magneto-resistive F.W. Bell NT-5 current sensor. The output of the sensor is a voltage proportional to the measured current. The output voltage range meets the electrical standards of the analog input of the analog IO board of the main computer of the MASS, so it can be directly connected to it.

As seen in Figure 3.2, the current sensor is connected in series with the variable load, being switched by the same switching relay connecting both solar cell sets. Therefore, a single sensor for current measurement is used, allowing to get comparable measurements and thus avoiding potential differences between sensors.

#### c) Voltage Measurement

The electrical implementation for voltage measurement is specific for the particular set of solar cells that are being tested, which is dependant on the expected maximum output voltage of the solar cells. The system must be designed so sensed voltages never exceed the electrical limits of the A/D converter. Higher-expected voltages occur during high irradiance episodes during open-circuit conditions.

In the case of silicon solar cell sets the open-circuit voltages will never exceed the maximum voltage accepted by the analog input of the AD board. Due to its low impedance, the voltage signal is directly feeds the analog input of the AD board.

Conversely, ATJ cells operate at higher voltages and lower currents than silicon solar cells due to its construction characteristics, as seen in section 2.4. These voltages exceed the maximum voltage limit allowed by the analog input. In order to decrease this input voltage a high-impedance voltage divider is implemented, obtaining a scaled value with negligible power losses. This high-impedance voltage

divider exceeds the maximum input impedance recommended for the analog input of the AD board. Therefore, a voltage follower is also included in order to decrease the input impedance observed by the AD input. Furthermore, a low-pass active filter was also incorporated to remove eventual noise in the signal. Voltage divider, low-pass filter and voltage follower are grouped and built together in a custom-built “signal conditioner” board (See Figure 3.2).

The main computer logs several voltages across each solar panel. The system logs voltages  $V_a$ ,  $V_b$  and  $V_c$  from the silicon solar cell set and scaled  $V_1$ ,  $V_2$  and  $V_3$  voltages for the ATJ solar cell set, according to the voltage sensing outputs shown in Figure 3.2. All voltages are measured using a single analog to digital converter located on the AD board, which combined with an internal multiplexer allows to measure several inputs sequentially. This method ensures that all voltages are measured with the same calibration/conditions of one sensor, thus making them comparable.

#### d) Solar Cell Temperature

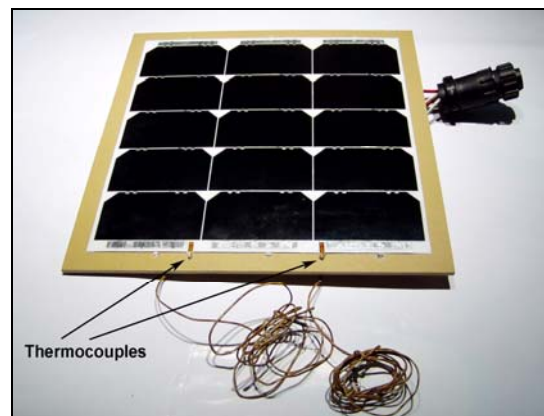


Figure 3.3: ATJ solar cell set used in the SCTU (embedded thermocouples are shown)

Each set of solar cells includes two K-type thermocouples located in two different locations of the solar panel as shown in Figure 3.3 for the ATJ solar panel

(location is analogous for the silicon solar panel). The system uses an ICP DAS CON I-7018 temperature transmitter to interface with the thermocouples, providing a calibrated output temperature upon request from the main computer of the MASS. The device digitally transmits the temperature values from the four thermocouples.

### **3.1.2 Pointing System**

The objective of the pointing system is to characterize testing solar cells under different external orientations. The solar cells and complementary instruments are mounted on a mobile platform controlled by a pan/tilt unit (PTU), as seen in Figure 3.4. The system can vary its orientation from horizontal to sun-pointing or any other fixed direction at any given moment. This mechanism provides the tools to quantify the power benefits of implementing a sun-tracking system for applications such as robots. It may be additionally used to determine the influence of the incident sun-angle over the efficiency of the solar cells due to reflections and varying path-lengths on each semiconductor caused by changes in the angle of the incident light.

The main component of the solar-tracking system is its operation software. Sun position is analytically determined knowing the geographical location and current date. Sun-tracking software is based on the SPICE<sup>4</sup> library written by NASA. SPICE system is used as the mechanism for capturing, archiving and disseminating a variety of ancillary and engineering information needed by scientists involved in space missions. SPICE ancillary data includes target body ephemerides and target size/shape/orientation (among other data) that allows to determine the position of the sun when provided with the geographic location (latitude and longitude) and current date and time.

---

<sup>4</sup> SPICE is the standard for nearly all NASA planetary missions such as Galileo, Clementine, MGS, Mars Odyssey, Cassini, NEAR, DS-1, Stardust, MER, Deep Impact, MRO and CONTOUR. It will also be used on Mars Express (in parallel with ESA standards), and it could be used on ESA's Rosetta, Japan's Nozomi, or other foreign missions.



Figure 3.4: SCTU mobile platform pointing to the sun

The SCTU uses a commercial Directed Perception Model PTU-C46-70 pan/tilt unit based on stepper motors. It includes a PTU controller which is operated using a standard RS/232 serial line of the main computer. The PTU has a freedom of 300° pan, 46° tilt (bottom) and 31° tilt (top). The pan range allows to track the sun during daylight, but the tilt range may be a limiting factor on certain locations at specific times of the day. The SCTU was built to operate in the latitudes ranging from the Atacama desert to Rancagua, Chile, where the sun is positioned in the range of the PTU during all the relevant high-irradiance times of the day for the whole year.

### 3.1.3 Auxiliary Sensors

The main objective of the auxiliary sensors is to capture data that characterizes the environment affecting the solar cell performance. All data is periodically captured and retransmitted for logging in the main computer. The most relevant onboard measurements are the irradiance (power per area) and solar spectra. Additionally the environmental temperature, relative humidity and wind speed are also logged. The described system is implemented using a general-purpose data logger and a spectrophotometer which are operated from the computer through a RS-232 line.

#### a) Data Logger Sensors

The system includes a Scientific Campbell CR10X general-purpose data logger. This is a programmable device able to interface with an enormous variety of

sensors for different purposes. Its interface offers analog inputs, pulse counters, switched voltage excitations and digital ports. The system runs user-programs (built with a proprietary programming language), being able to scan measurements at independent intervals and perform complex operations such as averaging of measurements and raw data conversion to standard units.

Table 3.1: Main characteristics of the SCTU sensors connected to the general-purpose data logger

Sensor	Main Characteristics
Pyranometer <i>Kipp and Zonen            CM3</i>	<ul style="list-style-type: none"> <li>-Thermopile pyranometer</li> <li>-Flat spectral response for the full solar spectrum</li> <li>-Spectral Response Waveband: 305 – 2800nm</li> <li>-Maximum Irradiance: 2000 <math>W / m^2</math></li> <li>-Operating Temperature: -40 to 80°C</li> <li>- Sensitivity: 23 <math>\mu V/W/m^2</math></li> <li>- 180° FOV</li> </ul>
Wind Monitor <i>R.M. Young 05103</i>	<ul style="list-style-type: none"> <li>-Measures wind speed &amp; direction</li> <li>- Range of operation (speed): 0 – 60 m/s</li> <li>-Accuracy (speed): 0.3m/s</li> <li>-Range of operation (direction): 355° (electrical)</li> <li>-Accuracy (direction): 3°</li> </ul>
Temperature & Relative Humidity Sensor  <i>Campbell Scientific            CS500-L</i>	<ul style="list-style-type: none"> <li>-Temperature Range: -40°C to 60°C               <ul style="list-style-type: none"> <li>- Expected error: &lt; 0.6°C for 0-35°C range</li> </ul> </li> <li>-Relative Humidity Range: 0 to 100%               <ul style="list-style-type: none"> <li>- Typical long-term stability: &lt;1% RH per year</li> </ul> </li> </ul>

The most relevant sensor for solar characterization attached to the data logger is the pyranometer, which senses the global irradiance with a 180° field-of-view. This data is used to calculate the conversion efficiency of the solar cells. As secondary instruments, a wind sensor and temperature / relative humidity sensor are also included. Table 3.1 details the sensors connected to the general-purpose data logger used by the SCTU and their main electrical characteristics.

#### b) Spectrophotometer

The system includes an Ocean Optics SD2000 spectrophotometer that allows to analyze the performance of the solar cell sets, capturing the incident solar spectra. The device was mounted on the same mobile-platform of the testing solar cells (controlled by the PTU) in order to determine the spectral shape of the incident solar radiation to the panels.

The spectrophotometer was incorporated mainly to analyze the performance of ATJ solar cells when comparing results to existing studies in space. ATJ solar cells are constructed including three junctions in series which capture specific parts of the spectra, as seen in chapter 2.4. If the atmosphere eventually filters relevant wavelengths to one of the junctions, the performance of the whole solar cell may be degraded due to its serial configuration. Therefore, spectral differences in space and in the atmosphere may be used to analyze the obtained results.

The spectrophotometer is powered and operated through a USB interface. It uses a closed proprietary communication protocol, so its operation is restricted to the tools provided by the manufacturer. It has two independent channels (master and slave) which together cover a spectral range from 200 to 1100nm. Although the spectrometer does not cover the complete spectral range used by ATJ solar cells (300 to 1900nm, approximately), it includes the part with highest irradiances (visible region).

### 3.1.4 Physical Layout

All devices related to the SCTU are mounted using the mounting system module provided by the MASS. Sensors, temperature transmitter and solar cells for testing are installed on a platform on top of the MASS tripod (see Figure 3.5).

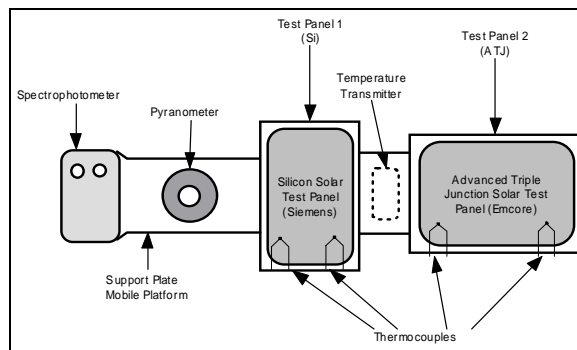


Figure 3.5: Top-view mechanical layout diagram of SCTU mobile platform

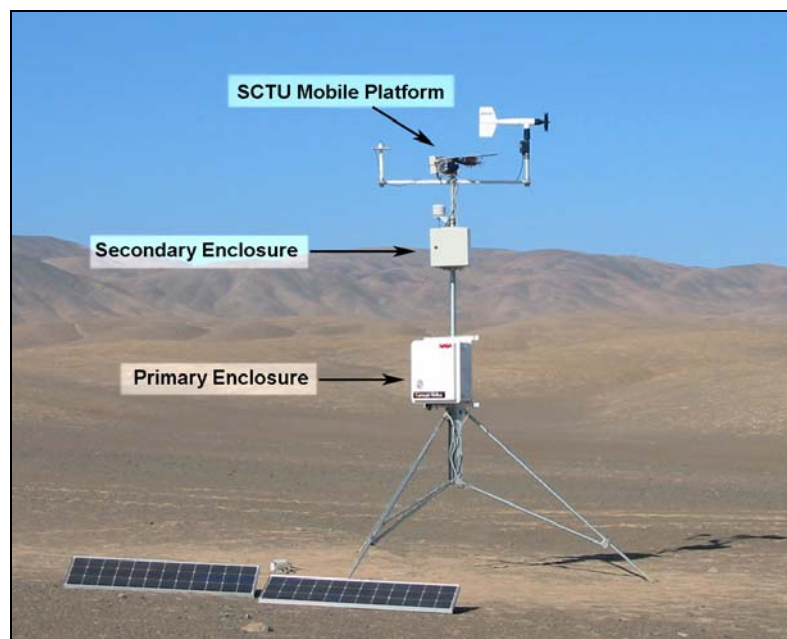


Figure 3.6: Main components of the MASS/SCTU mounted in the field

Most of the electronics within the SCTU, including the signal conditioner board, PTU controller and general-purpose data logger are mounted in the MASS electronics enclosure. A SCTU-specific secondary electronics enclosure was installed on top of the tripod in order to place the variable load as close as possible to the test solar cells. This minimizes cable length requirements of the solar cells/variable load circuit, minimizing undesired inductive noise and resistive losses.

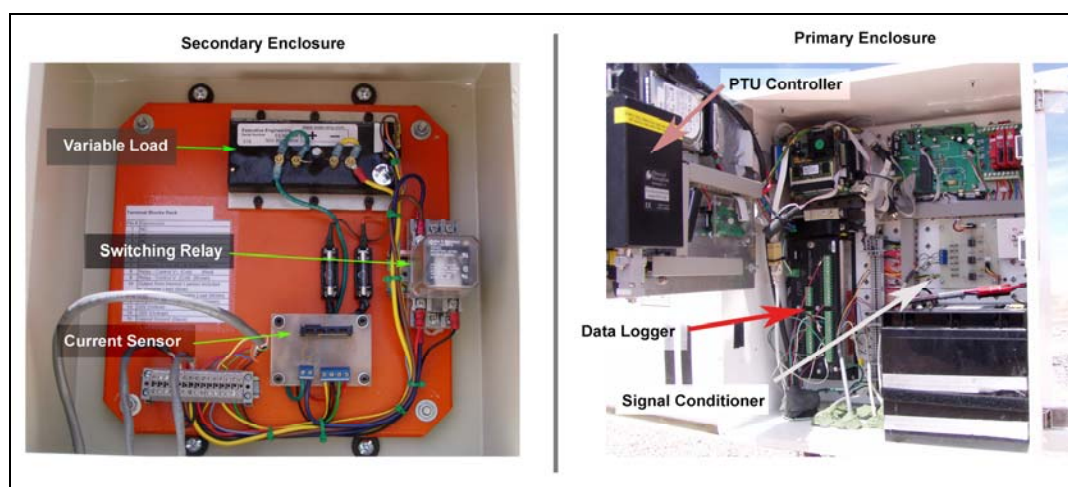


Figure 3.7: Layout of components in the Primary and Secondary Electronics Enclosure

Figure 3.6 shows the mounting scheme of the SCTU. Figure 3.7 shows the layout of components of the SCTU in the primary and secondary electronics enclosures.

### 3.1.5 Control Software

The control software of the SCTU runs on the main computer of the MASS capturing and organizing data. It operates the general-purpose data logger, temperature transmitter, PTU controller and main experiment using the interfaces of the main computer. The system uses RS/232 serial interfaces for communications with the general-purpose data logger, temperature transmitter and PTU controller; digital outputs to control the relay in order to switch to the appropriate solar-cell set; analog outputs to operate the variable load; and analog inputs to read current and

voltage levels. The system generates ordered logs with the captured data and also Octave<sup>5</sup>-formatted scripts to create plots that need to be created on a regular basis.

a) General Operation of the software

The main objective of the SCTU software is to capture data from the main experiment and auxiliary sensors under various orientations defined in the pointing system. The user selects custom *predefined positions*, which are definable orientations of the solar cell sets where the electrical tests will be performed. Predefined positions may be composed of fixed positions or by the sun-tracking system operated by the SPICE library of NASA described in section 3.1.2.

The system runs a loop which periodically executes a set of experiments including logging current, voltage and temperature data for the complete range of operation of each set of solar cells in all predefined positions. Therefore, during each loop the software powers-up the PTU, points it to the first predefined position and controls the variable-load to operate the first set of solar cells from open-circuit to short-circuit. Once it has finished, it switches the load to the second set of solar cells and repeats the experiment. The PTU is sequentially pointed to each of the following predefined positions, repeating equivalent experiments for each position for both solar cell sets. Finally the PTU is powered-down until the next set of experiments is performed.

The software samples the temperatures of the four thermocouples attached to the solar cells for each I-V pair acquired. Also the global irradiance acquired by the pyranometer is logged for each predefined position.

A summary of the complete procedure when obtaining a set of experiments is summarized as a flowchart in Figure 3.8.

---

<sup>5</sup> Octave is a free software written under the terms of the GNU General Public License (GPL) by John W. Eaton and others. The software is a high-level language, primarily intended for numerical computations with capabilities similar to Mathworks Matlab®.

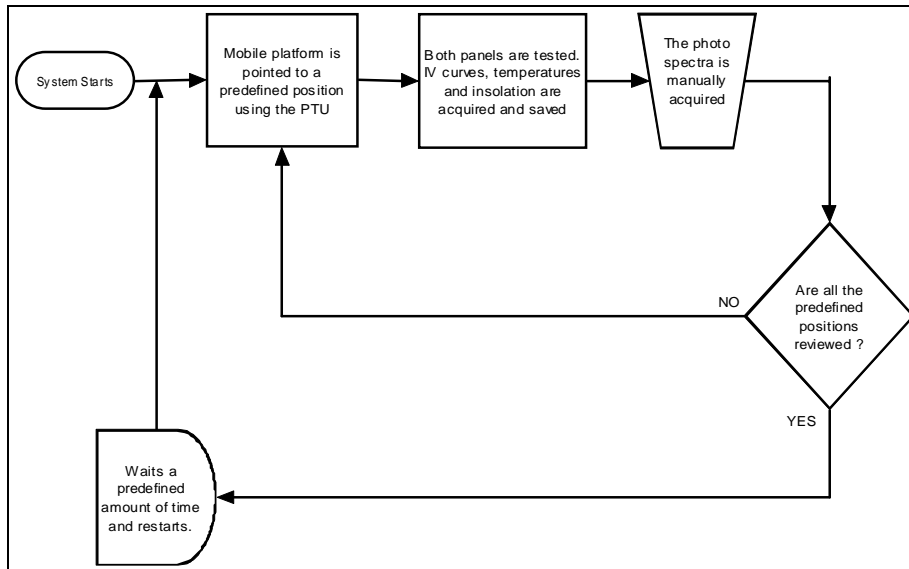


Figure 3.8: Flowchart of the general software operation

#### b) Software of the electronically-controlled load

As noted in section 3.1.1 the variable-load is controlled via its current manipulation. Therefore, a constant control signal will draw a constant amount of current independent of the load voltage. As a consequence, the control voltage required to reach the short-circuit condition is not constant, and is dependant on the characteristics of the solar cells used.

The SCTU software generates a voltage control-signal in incremental steps in order to vary the solar cell operation from open-circuit to short-circuit conditions. The system logs only data points that provide valuable information, i.e. points which are obtained until the short-circuit condition is reached. The short-circuit condition input voltage is empirically determined for the specific set of solar cells that are being tested. This parameter which is introduced in the programming code. As a consequence in the SCTU, silicon and ATJ solar cell sets have dedicated connectors that cannot be interchanged. Furthermore, the programming code will need modifications (and recompilation) if new solar cell sets with different electrical characteristics were incorporated to the system.

c) Data processing

The SCTU process automatically generates Octave plot scripts that generate commonly-used graphs on a daily-basis. Generated plots include weather plots, the current-voltage curve (highlighting the maximum power point), and any other custom relevant variable defined by the user.

d) Auxiliary process for manual operation

The system includes a complementary (and optional) process, independent from the SCTU software previously described in order to manually operate the SCTU. This auxiliary process must be manually executed by the user by logging into the main computer of the MASS. The user gains direct control over the SCTU being able to point the solar cells at arbitrary positions and to execute experiments at any given moment. This manual execution is useful when the user wants to perform the experiments at precise intervals with particular external conditions, and to take external manual measurements such as spectra for certain precise orientations.

### **3.2 Environmental Conditions during Experiments**

a) Location

The SCTU was installed in a rural zone in the O'Higgins regions, near the Punta de Codegua Village Chile. The geographic coordinates of the location are latitude 34° 00' S longitude 70° 39' W.

b) Date

To ensure the same testing conditions for all the collected data, experiments were acquired during a single day on December 12, 2004. The selected day was a "typical" summer day on the area, sunny and completely cloudless. The experiments were repeated approximately every 45 minutes. The first experiment started at 11:05 and the last ended at 18:30; Each experiment lasting no more than 10 minutes.

## c) Irradiance

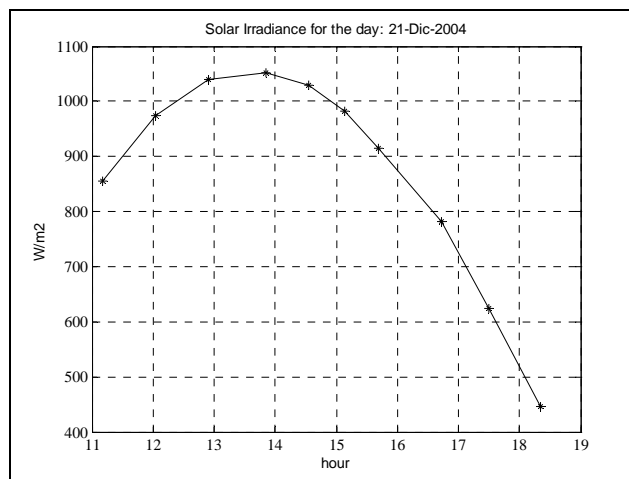


Figure 3.9: Solar Irradiance of the Day

The instantaneous solar irradiance was captured for the analysis of the solar cells immediately after current-voltage curve measurements on each predefined position. Figure 3.9 shows the solar irradiance for the testing day with the pyranometer in horizontal position, where each point represents an individual experiment. The maximum measured insolation occurs during the fourth experiment at 13:51, reading  $1052 \text{ W/m}^2$ . This time almost coincides with the moment in which the sun was nearest to the surface of the earth which occurred at 13:40 hours.

### 3.3 General Considerations Used for Data Analysis

This section contains some considerations that apply to all the results presented in this document.

Since each panel has several solar cells, I-V curves presented in this document are average values from the individual solar cells of each panel. This methodology ensures representative results for the corresponding technology, and not of an individual solar cell.

The vertical axis of the I-V curves plots display current densities (J, current per unit area) instead of total current, allowing direct performance comparisons between both solar cells types, which have different surface areas.

Temperature compensations and corrections are achieved using the temperature coefficients provided by the solar cells manufacturers. The accuracy and precision of these values were not verified because it is not possible to control the temperature of the solar cells with the SCTU.

## 3.4 Results

### 3.4.1 Overview of Electrical Characteristics

To illustrate the general electrical behavior of the ATJ and silicon solar cells, typical I-V curves are shown in this section. The curves were acquired during the maximum insolation episode of the testing day, with the solar cells deployed horizontally.

#### a) I-V Curves

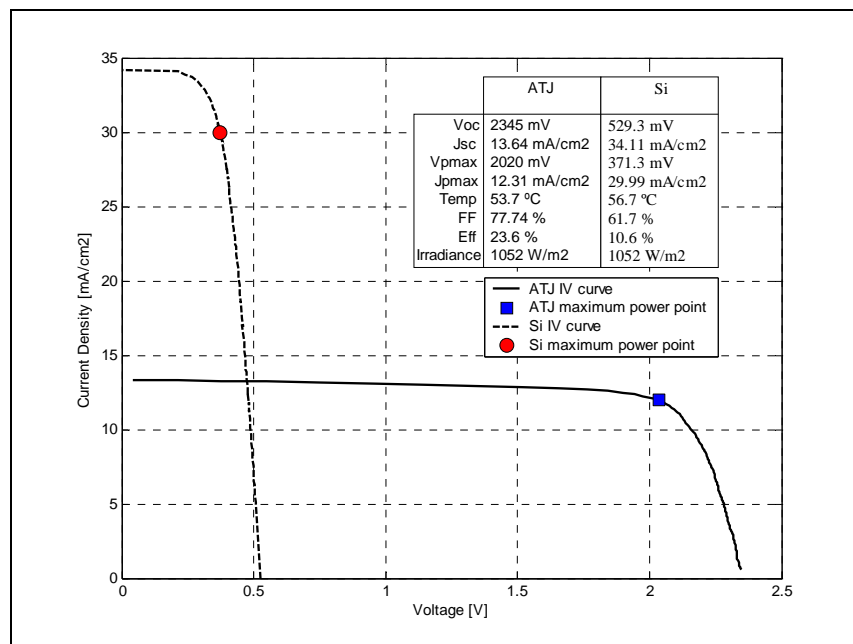


Figure 3.10: I-V Curves of ATJ and Si solar cells

Figure 3.10 displays the average I-V curves for the ATJ and silicon solar cells sets.

## b) Comparison of Electrical Characteristics

A quick view of both curves corroborates that the electrical characteristics differ significantly between the two solar cell types.

### i) Maximum Efficiency Operation Point

The voltage at maximum power ( $V_{pmax}$ ) of ATJ solar cells is 2 volts, more than 5 times the  $V_{pmax}$  of the Silicon solar cells which is only 0.37 volts. On the other hand, the maximum-power current-density ( $J_{pmax}$ ) of ATJ solar cells is 12.3 mA/cm<sup>2</sup>, less than half of the  $J_{pmax}$  of the silicon solar cell which is 30.0 mA/cm<sup>2</sup>. These operating conditions are confirmed by the theory of the multi-junction solar cells (described on Chapter 2.4), which states that multi-junction cells deliver higher voltages and lower currents than single-junction solar cells.

Comparing the power output per area of silicon and ATJ solar cells at their maximum efficiency points, the ATJ delivered **249 W/m<sup>2</sup>** in contrast with **111 W/m<sup>2</sup>** for the silicon solar cells. This means that the ATJ converts **2.2** times more power. In relation to conversion efficiencies, the ATJ achieves 23.6 % and the silicon 10.6%. The ATJ maintains the same advantage in ratio of 2.2 over the silicon solar cell, since the solar irradiance value is constant for both experiments.

### ii) Shape of the I-V Curve

Another interesting difference between both solar cell types is the shape of their I-V curve. While the ATJ curve has a more squared shape (sharp corner), the silicon curve is rounder. This peculiarity is reflected by the Fill Factor (FF) parameter, which is 77.7 % for the ATJ, and 61.7% for the silicon solar cell. The higher fill factor of the ATJ means that the  $I_{pmax}$  and  $V_{pmax}$  will not change significantly from the  $I_{sc}$  and  $V_{oc}$  values, delivering a more regulated output, less dependant on the load, than the silicon solar cell.

### 3.4.2 Performance Under Varying Conditions

#### a) Causes of Varying Conditions

I-V curves displayed on section 3.4.1 only reflect the performance of the solar cells on a particular instant of the day. To reveal the change in performance along the day, several I-V curves must be compared. Differences in the I-V curves are caused by several factors, including variations in the temperature of the solar cells and changes of the incident radiation, among others. Variations in the incident radiation are mainly caused by changes in the angle of incidence of the sun radiation and differences in the path lengths of sunrays crossing the atmosphere.

#### i) Angle of Incidence

The performance of the solar cell is dependant on the relative position of the sun to its surface (projected area). This relative position is dependant on the zenith and azimuthal angles<sup>6</sup> which describe the path of the sun on the surface of the earth.

A direct consequence of the varying incident angle on the solar cell is the radiometric *cosine effect*. This effect states that for a surface located on a fixed position on earth the amount of incident sunrays will vary along the day due to variations of the exposed area to the solar rays<sup>7</sup>. The maximum amount of incident radiation on the fixed surface will occur when the incident sunrays strike perpendicular to the fixed surface. This occurs because during these episodes the

---

<sup>6</sup> The zenith angle defines the position of the sun relative to a line which is perpendicular to the surface of the earth at the location. The azimuthal angle describes the position of the sun relative to the north-south axis.

<sup>7</sup> This approach considers that all the incident light to the surface is due to direct normal irradiance (beam irradiance), neglecting the amount of incident diffuse radiation (reflections of scattering)

parallel incident sunrays “see” the largest surface (source projected area over surface is maximum).

ii) Influence of the atmosphere

The path length of the incident radiation crossing the atmosphere varies with the position of the sun. Normal incident sunrays to the surface of the earth cross a small section of the atmosphere, resulting in less attenuation. Conversely, when the path of the sunrays is largest, the attenuating effect of the atmosphere on the sunrays increases, resulting in a lower irradiance on the surface of the earth. These path length differences also cause variations in the solar spectra, since the atmosphere absorption is wavelength dependant.

iii) Solar cell operation temperature

Performance of PV devices is also dependant on the temperature of the solar cell. Considerable deviations are expected for I-V curves obtained under equivalent conditions but with significant temperature differences, such as those existing in space and earth.

In order to compare the operation of solar cells under different conditions, manufacturers provide accurate temperature correction coefficients for voltage and current values ( $\Delta V / ^\circ C$  and  $\Delta i / ^\circ C$ , respectively) for their solar cells. These factors allow to cancel the effects of temperature when analyzing its influence on the solar cell performance.

b) Measured I-V curves

Figure 3.11 shows three different I-V curves (morning, afternoon and maximum irradiance episode) for each of the tested solar technologies. These values were acquired with the solar cells located on a fixed horizontal position during the cloudless testing day.

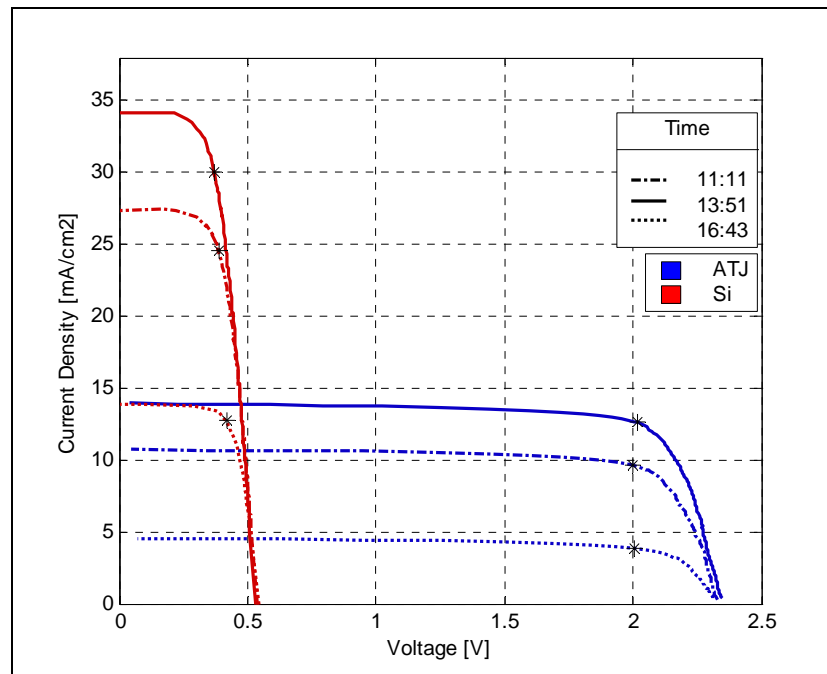


Figure 3.11: I-V curves along the day for the ATJ set (blue) and silicon set (red). Horizontal position. Maximum power points are marked by an asterisk (\*)

I-V curves shown in Figure 3.11 along the testing day are the actual values measured at the field, which include all degrading effects recently discussed (temperature, cosine effect and variations in the path length of the incident radiation).

Obtained curves show large differences in the short-circuit current ( $I_{sc}$ ) and similar open-circuit voltages ( $V_{oc}$ ) along the day. Significant differences in current at low voltages are expected because current values are proportional to the incident irradiance, generating lower values at early and late times of the day. On the other hand,  $V_{oc}$  values were expected to converge to a single point, which probably did not occur due to temperature and spectral issues which will be discussed in the following sections.

- c) Compensation to a single solar cell temperature: influences of the atmosphere and cosine effect

Figure 3.12 shows the same I-V data displayed on Figure 3.11 but with each data point temperature-corrected to operate at 28 degrees Celsius according to the temperature logged for each current-voltage pair. Significant variations can be observed in the curves respect to the raw measured values in Figure 3.11, with changes consisting mainly on a displacement of the voltage values. Additionally, variations of the open-circuit voltage persist, suggesting that the causes are not related to temperature variations.

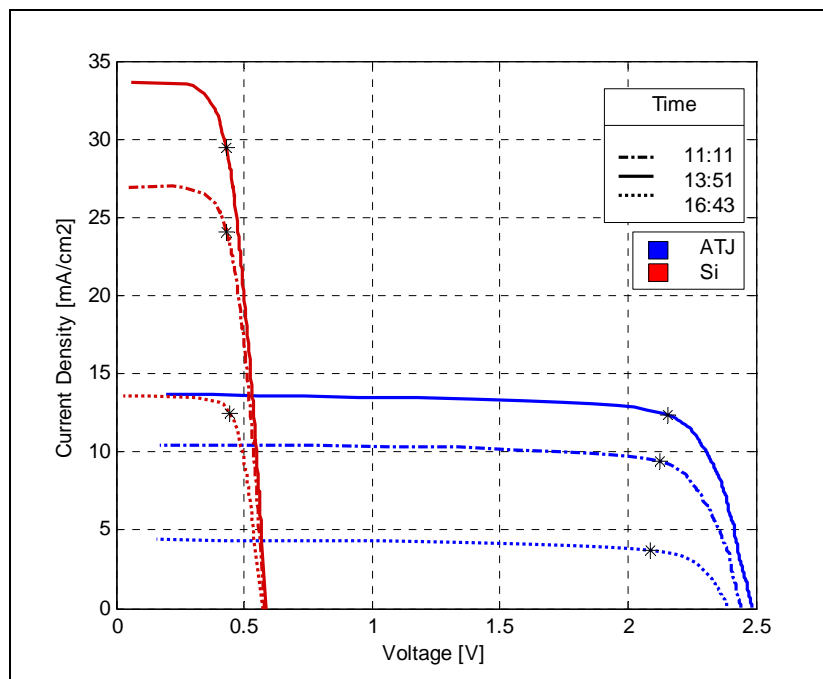


Figure 3.12: I-V curves along the day with temperature compensation (28°C) for the ATJ set (blue) and silicon set (red). Horizontal position. Maximum power points are marked by an asterisk (\*)

Displacement of values are caused because the voltage outputs of the solar cells are inversely proportional to temperature and on the contrary, current outputs are directly proportional to temperature. There is a significant change in the operation temperature of the solar cells along the day as seen in Table 3.2, obtaining the maximum value during the maximum insolation instant. Therefore, the

performance degradation caused by high temperatures is higher during experiments performed during high-irradiance episodes. Figure 3.12 eliminates the interceptions seen on Figure 3.11 because it compensates for the degradation seen during these high-irradiance episodes, generating the corrected values for the solar cell if the temperature would have been kept constant for all three.

Table 3.2: Average temperature of solar cells under horizontal position testing

Time	ATJ	Silicon
11:11	49.1 °C	49.9 °C
13:51*	53.7 °C	56.7 °C
16:43	52.8 °C	53.7 °C
<i>Average</i>	<i>51.9 °C</i>	<i>53.4 °C</i>

\* Max insolation instant

The temperature compensated curves in Figure 3.12, reflect that changes along the day are caused by variations in the incident radiation to the solar cells (neglecting secondary effects that cause minor performance changes, which are not addressed in this work). Therefore, changes in the I-V relationships during the day (Figure 3.12) are caused mainly by the cosine effect and by variations in the path length of the incident radiation.

#### d) Cancellation of the Cosine Effect: The Atmosphere Absorption Effect

As earlier discussed, the cosine effect is the result of variations in the projected surface (in this case the solar cell sets) to the incident sunlight due to the movement of the sun. Therefore, implementing a mobile system that maintains the relative position of the sun constant respect to the solar cells would cancel the cosine effect. Figure 3.13 shows the result of an equivalent experiment as the one reported by Figure 3.12, but implemented on a continuous solar-tracking system.

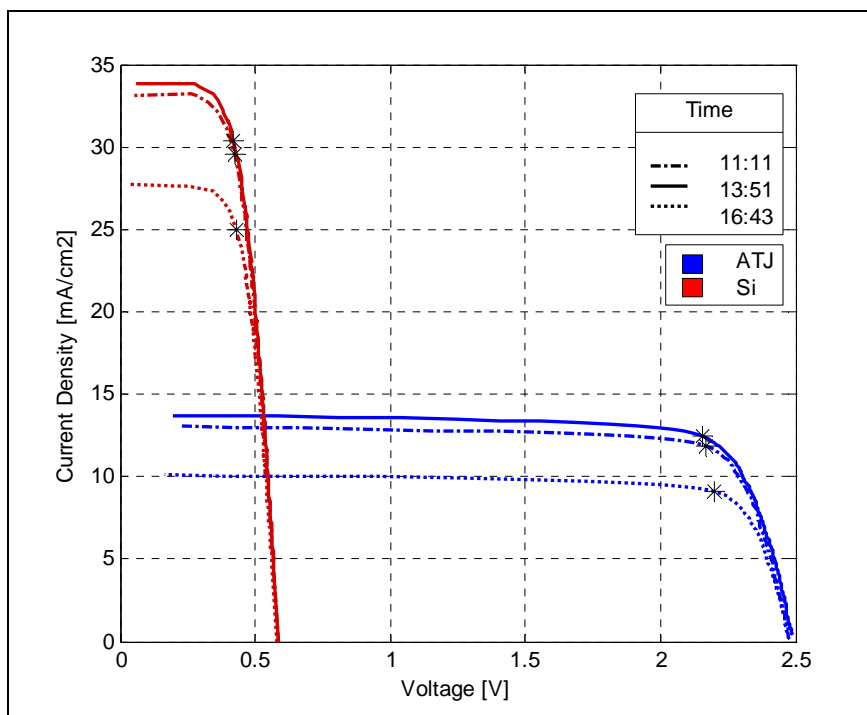


Figure 3.13: I-V curves with sun tracking and temperature compensation for the ATJ set (left) and silicon set (right)

This tracking system keeps the relative position of the sun normal to the surface of the solar cells at all times. Therefore, variations of the I-V curves along the day (Figure 3.13, also temperature compensated at 28 degrees Celsius) are only the result of variations in the path-length of the incident radiation along the testing day.

Due to the cancellation of the cosine effect the global performance of both solar cell technologies increase significantly, specially during times of the day where the zenith angle is relatively small. As expected, the cosine effect virtually does not affect the performance of the solar cells during the high-irradiance episode of the day because the zenith angle is virtually normal to the horizontal position of the solar cells (the efficiencies variations will be addressed in depth in the next section).

The cancellation of the cosine effect causes the open-circuit voltage to converge to a single value for both solar cell technologies. Therefore, variations of the open-circuit voltage point identified in Figure 3.11 and Figure 3.12 are likely caused by the reflection or filtration of specific wavelengths on one of the upper layers (such as the anti-reflection coating), due to “unfavorable” incident angles. These missing wavelengths are not captured by the semiconductor causing a degradation of performance of the solar cell.

#### e) Changes in Conversion Efficiency

Conversion efficiency is sensitive to sun radiation conditions and solar cell temperatures. To understand the influence of these factors, first the efficiencies of the solar cells along the day are displayed and then, the effect of each factor is analyzed.

##### i) Efficiency Variations Along a Single Day

Figure 3.14 shows the conversion efficiencies of the solar cells at different times during the trial day, (11:00AM to 6:30 PM), with the solar panels positioned horizontally. Statistics of the conversion efficiencies and fill factors along the testing day are presented in Table 3.3.

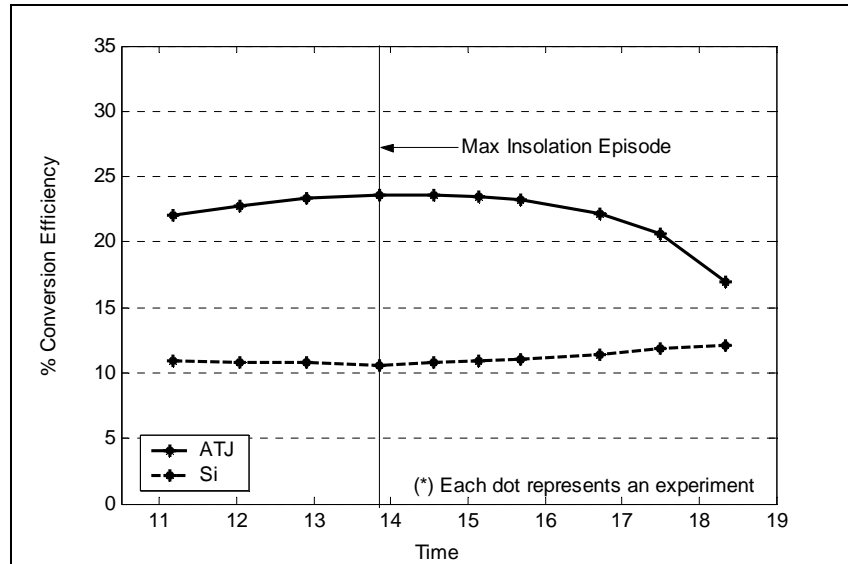


Figure 3.14: Conversion efficiencies during test day

Table 3.3: Conversion Efficiencies and Fill Factors

		ATJ	Si
<b>Conversion Efficiency</b> $\eta\%$	Average	<b>22.2</b>	<b>11.1</b>
	<i>Max</i>	23.6	12.1
	<i>Min</i>	17.0	10.6
<b>Fill Factor</b> %	Average	<b>77.2</b>	<b>63.4</b>
	Std. Dev.	0.01	0.03

Results confirm that there is an important variation in the conversion efficiencies along the day. On the other hand, the fill factors remain almost unchanged.

## ii) Effect of the Angle of Incidence

To establish the influence of the angle of incidence, the solar panels were tilted to different orientations under constant irradiance conditions. To isolate other factors only the data from a single experiment is used, ensuring that the incident spectra and direct/diffuse irradiance ratio has not varied. This is assumed since the measurements involved last no more than ten minutes, therefore the radiation conditions are considered approximately constant. Also, the data is temperature compensated to 28 degrees Celsius.

Figure 3.15 displays the degradation of the conversion efficiencies under different angles of incidence of the radiation of the sun over the ATJ solar cells. The results were obtained from four distinct orientations, which are: pointing to the sun, horizontal, and zenith angles of 34° and 44° facing to the north (Azimuth 0°). The experiment was performed between the 15:05 and 15:16 hours during the testing day.

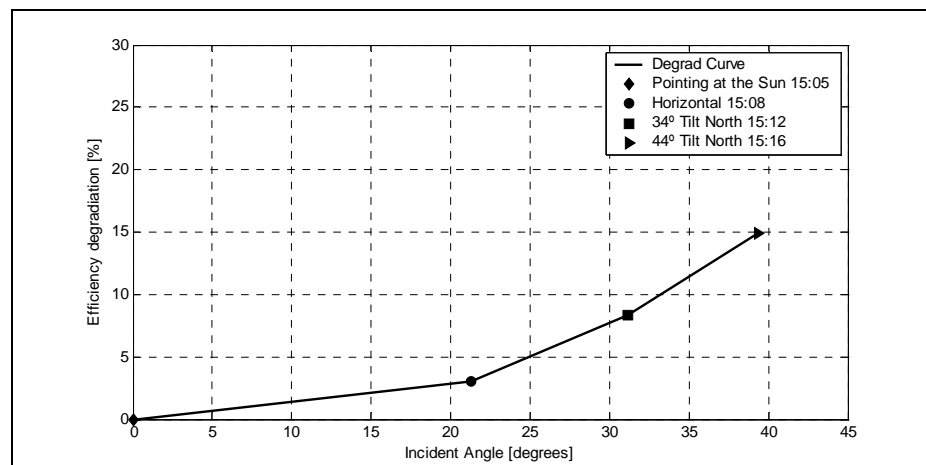


Figure 3.15: Efficiency degradation with respect to the angle of incidence of the radiation for the ATJ solar cells

Figure 3.15 confirms that the angle of incidence of the direct sunlight beam over the ATJ solar cells has a significant effect over the conversion efficiency. This factor explains the degradation of the efficiency of the ATJ solar cells along the day in horizontal position during the early and late hours. This is confirmed by Figure 3.16, which displays the efficiencies of the solar cells continually pointing to the sun versus positioned horizontally along the day. Comparison with a sun-pointing system is useful because the incident solar angle is kept normal to the surface of the solar cell. The plot clearly demonstrates that the efficiencies are more constant when pointing to the sun, contrary to the horizontal position where they are sensitive to the time of the day since the angle of incidence changes.

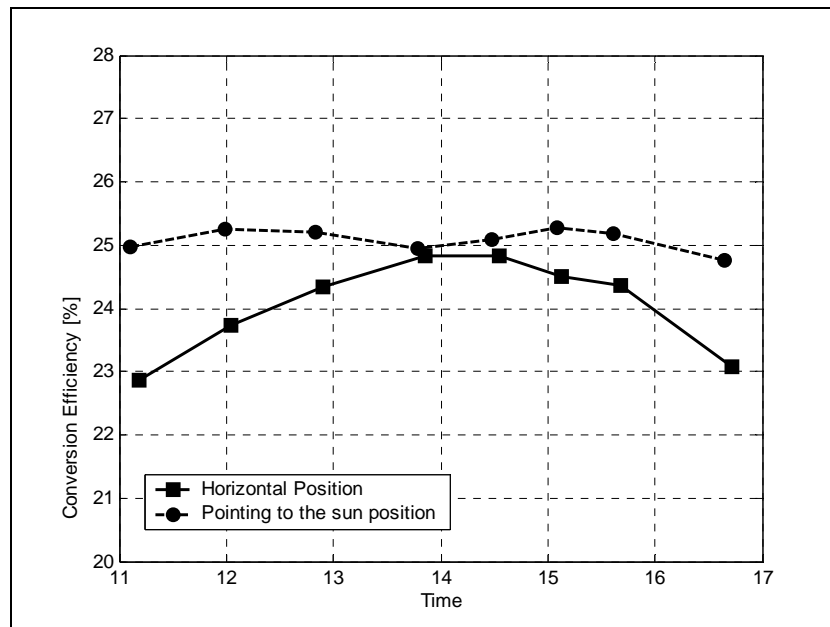


Figure 3.16 : Efficiencies of ATJ solar cells in horizontal and pointing to the sun positions along the day.

Performance degradation with increasing angles of incidence may be caused by multiple factors. Among them, the most likely are reflections and increasing recombinations in the semiconductor.

ATJ solar cells are provided with broadband dual-layer antireflection (AR) layers. The materials and thicknesses of these layers are optimized to cancel reflections from a wide band of incoming wavelengths (see “Multi-Junction Solar Cells”, section 2.4.2). This optimization is only valid for angles of incidence that are close to zero degrees (normal to the surface). Incident radiation with larger angles will generate longer optical path lengths (OPLs) through the AR and semiconductor layers. In the AR system, these extended OPLs will change the reflectance distribution of the coatings along the different wavelengths, accordingly, the resulting reflectance distribution will differ significantly from the intended. This phenomenon causes a performance degradation since the three layers are current-matched for the spectrum filtered by the intended reflectance distribution. Furthermore, in the semiconductor layers the longer OPLs of the refracted rays will expose photons a longer time in the different layers. Consequently, some types of recombination are more likely to occur, in particular in the top and middle junctions of the ATJ cells, which are made of direct bandgap materials. See appendixes A and B (pages 65 and 68, respectively) for further details.

No significant degradation in performance was noticed in the silicon cells. In contrast with the flat surface of the ATJ technology, the silicon cell has micro-pyramidal textures in its surface, feature that increases the absorption of light from a broad range of angles of incidence. Additionally, silicon cells are not apparently influenced by the extension of the OPLs of the light inside the semiconductor layers. This occurs given that silicon is an indirect bandgap material, therefore certain types of recombinations are less likely to occur.

### iii) Effect of Temperature

In order to determine the effect of temperature in the conversion efficiency, the data is compensated to different temperatures to observe the variations of the conversion efficiency.

The results of this theoretical exercise are shown in Figure 3.17, where the temperature is varied from 0° to 80° Celsius with the solar panels positioned horizontally. The results were obtained using the temperature coefficients provided by the manufacturers, which in both cases are constant. From the plot it can be

observed that in the case of the ATJ cells, efficiency variations due to changes in temperature are lower during late hours than for silicon cells. This occurs since the ATJ solar cells generate significantly less current during late hours. At higher temperatures, these weak current values are considerably increased by temperature compensation factors (which only depend on the temperature) in such a way that is proportional to the voltage decrease (by temperature compensation), thus maintaining the generated power constant. This phenomenon is also noticed in the silicon cells, but is less evident given that the currents are more stable along the day .

Observing Figure 3.17 it can be inferred that the increase in performance of the silicon cells in the late hours is not due to temperature variations, since each curve is compensated to a single temperature value. This characteristic probably occurs due to favorable illumination conditions, which include changes in the incident spectra and variations in the diffuse/direct irradiance ratio.

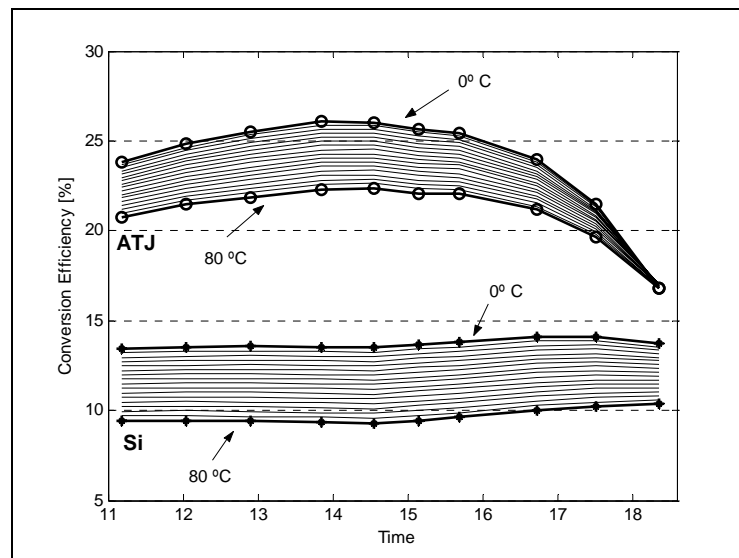


Figure 3.17: Efficiencies along the day, with different temperature compensations, from 0° to 80° C.

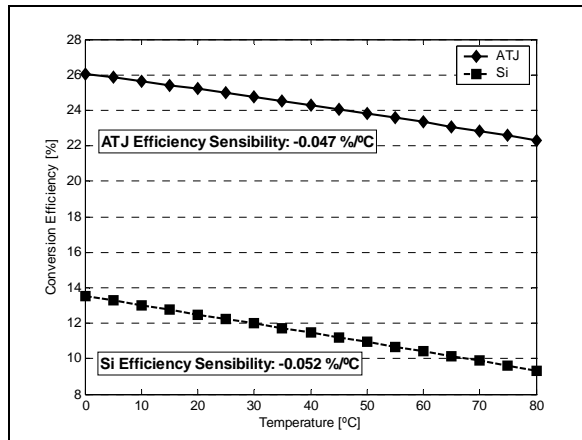


Figure 3.18: Conversion efficiency vs. temperature at maximum insolation instant.

Figure 3.18 shows the relationship between temperature and efficiency of the solar cells during the maximum insolation instant of the testing day. Since the efficiency versus temperature curves are almost linear during this time of the day, linear sensitivity factors are displayed in the plot. Both sensibility values are similar, being the ATJ technology slightly less sensitive to temperature.

### 3.4.3 Performance of ATJ Solar Cells on Earth versus Space

The manufacturer provides electrical characteristics for ATJ solar cells operating in space at an  $1353 \text{ W/m}^2$  (average, measured outside the atmosphere, called AM0 conditions), as shown on Figure 3.19 [12]. The tested ATJ solar cells are manufactured to maximize their performance under space conditions, therefore worse results are expected when operating on earth.

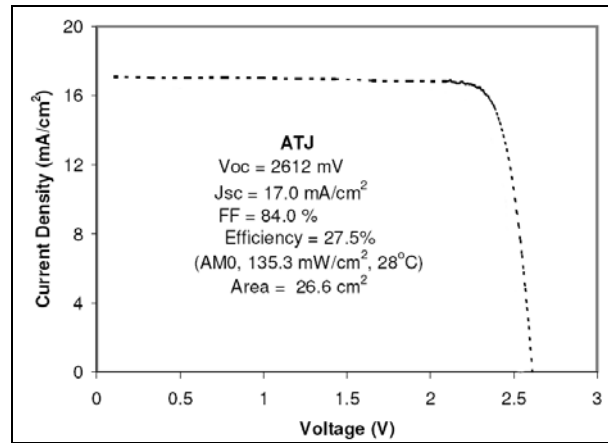


Figure 3.19: I-V curve of ATJ solar cells operating in space under AM0 conditions ( $1353 \text{ W/m}^2$ ) at  $28^\circ\text{C}$

Figure 3.20 displays the results of the ATJ solar cells tested on earth under the most favorable conditions on the testing day. These are obtained during the maximum irradiance instant of the day with the solar cells pointing to the sun, what constitutes the best possible effort on earth to “simulate” existing conditions in space. Table 3.4 summarizes the main electrical characteristics of ATJ solar cells operating in space and on earth.

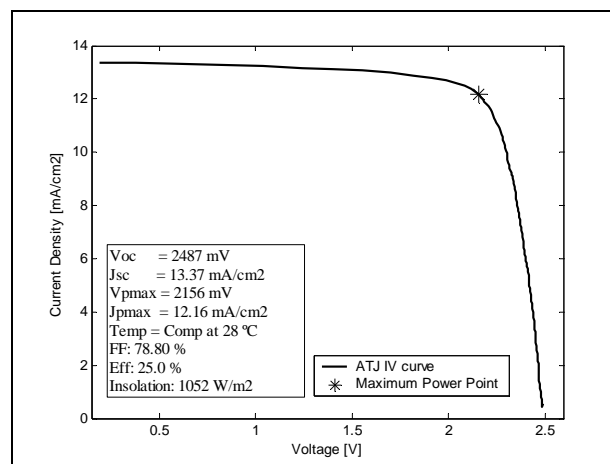


Figure 3.20: I-V curve of ATJ solar cells operating on earth, with the solar cells pointing to the sun, compensated at  $28^\circ\text{C}$

Table 3.4: Electrical characteristics of ATJ solar cells operating in space compared to operation on earth

	Operation in Space	Operation on Earth
Efficiency	27.5%	25.0%
Fill Factor	83.8%	78.8%
Open-circuit voltage ( $V_{oc}$ )	2.60V	2.49V
Short-circuit current density ( $J_{sc}$ )	17.1 mA/cm <sup>2</sup>	13.37 mA/cm <sup>2</sup>
Voltage at maximum power ( $V_{mp}$ )	2.30V	2.16V
Current density at maximum power ( $J_{mp}$ )	16.2 mA/cm <sup>2</sup>	12.16 mA/cm <sup>2</sup>

As expected, the operation of ATJ solar cells is degraded when operating on earth. The main causes are the large differences in the incident irradiance and in its spectral components. The maximum measured insolation on earth during the testing day was 1052 W/m<sup>2</sup>. Figure 3.21 contrasts the AM0 conditions with the spectrum measured during the testing day (the spectrophotometer used on the experiments covers a limited spectral range but includes the most energetic band of the spectrum).

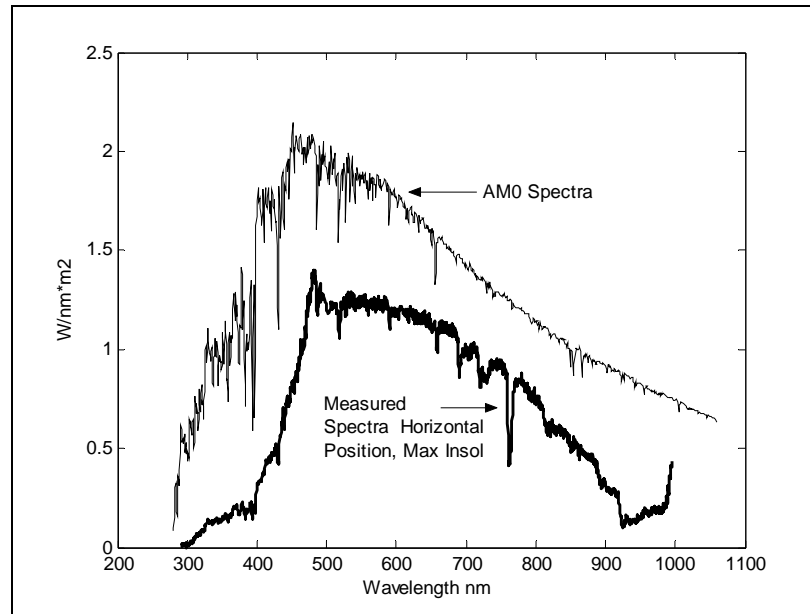


Figure 3.21: Solar spectra in space and on earth during experiments (Measured spectra was scaled for comparison purposes)

In the case of efficiency parameters, operation on earth is degraded in a 9% respect to operation in space, what anyway constitutes a high efficiency compared to traditionally-used technologies. This degradation in efficiency is significantly less than the 22% reduction in the global irradiance. This peculiarity is explained because the atmosphere unequally filters the incident light, and the contribution of individual wavelengths to the efficiency of the solar cell is not constant. Therefore, although globally the incident spectra is noticeably filtered, the most affected wavelengths have a relatively low incidence in the efficiency of the solar cell.

#### 4. CONCLUSIONS

This document has addressed the performance of Advanced Triple Junction (ATJ) InGaP/InGaAs/Ge solar cells, originally designed to operate in space, when used in terrestrial applications. Results are contrasted to the performance of conventional silicon solar cells, widely available in the worldwide market, under equivalent external conditions.

Experimental efficiencies obtained average 22.2%, reaching a maximum of 23.6% (or 25%, if compensated to 28° Celsius) during the most favorable conditions of the day. The results are significantly better than those obtained for conventional technologies. The ATJ cells doubles the efficiency of silicon solar cells under equivalent conditions.

It was proved that ATJ solar cells present a variable-efficiency characteristic which is dependant on the angle of incidence of the sunlight. Higher efficiencies are obtained when the sun is positioned normal to the solar cell. This characteristic differs to the obtained results for the silicon technology (which was built for use on earth), presenting no relevant efficiency deterioration with respect the angle of incidence. Consequently, the probable causes of the performance degradation of the ATJ cells are due to the extension of the optical path lengths (OPLs) in the antireflection (AR) coatings and semiconductor layers. These extensions become larger with wider angles of incidence. The increase of the OPL in the AR coatings minimizes the antireflection effectiveness, changing the reflectance distribution, for which the semiconductor layers widths where optimized (current-matching). On the other hand, the change of the OPL in the semiconductor section increases the time photons remain in the different layers, augmenting the probability of certain types of recombination. The factors mentioned above apparently do not influence the performance of the silicon cells. One of the possible reasons for that is that Si cells have micro-pyramidal top surfaces that capture light from wider angles of incidence. Also, silicon is an indirect-bandgap material, which is less susceptible to certain recombinations types that occur more often in the direct-bandgap materials of the ATJ due to longer OPLs in the semiconductor.

Although the ATJ cells performed remarkably better than the silicon cells, even better results are expected if they are fine-tuned for terrestrial use. This tune-up would include a better current matching strategy for the AM1.5 spectrum, and also if possible, the fabrication of a micro-pyramidal surface in the top of the cell.

Today, generation-costs per unit of energy is significantly greater for ATJ solar cells than for silicon technology, being 5.5 times more expensive per watt generated<sup>8</sup>. Therefore, although efficiencies of ATJ solar cells are considerably better than those of traditional technologies, economic constraints cause that the application of ATJ solar technology is only recommended where space-efficiency is important, such as in mobile vehicles and robots. It is expected that these costs drop in the future as the ATJ technology becomes a widely-available commercial product. As prices become more competitive, ATJ solar cells will probably start to replace current technologies due to its unquestionable better performance in most of the aspects tested in this work.

---

<sup>8</sup> Price of silicon solar cells was obtained based on the cost of a 36-cell Siemens SM55 commercial solar panel; price of ATJ solar cells corresponds to the cost of the tested solar cells based on a 1000-unit purchase. Efficiencies used to calculate this ratio were those obtained in this study.

## BIBLIOGRAPHY

- [Wett03] WETTERGREEN, D., CABROL, N., CALDERÓN, F., DEANS, M., JONAK, D., LUDERS, A., SHAW, F., SMITH, T., TEZA, J., TOMPKINS, P., URMSON, C., VERMA, V., WAGGONER, A. y WAGNER, M. (2003) **Life in the Atacama: Field Season 2003 Experiment Plans and Technical Results**. Carnegie Mellon University Robotics Institute. Technical Report CMU-RI-TR-03-50.
- [Angr82] ANGRIST, W. (1982) **Direct Energy Conversion**. (4<sup>th</sup> Edition) Allyn and Bacon, Inc. Boston.
- [Nrel00] National Center for Photovoltaics, **The Basic Physics and Design of III-V Multijunction Solar Cells**. NREL, NCPV. [http://www.nrel.gov/ncpv/pdfs/11\\_20\\_dga\\_basics\\_9-13.pdf](http://www.nrel.gov/ncpv/pdfs/11_20_dga_basics_9-13.pdf).
- [Fraa01] FRAAS, L., DANIELS, W., HUANG, X., MINKIN, L. AVERY, J., O'NEILL, M., MCDANAL, A. y PISZCZOR, M. (2001) **34% Efficient InGaP/GaAs/GaSb Cell-Interconnected-Circuits For Line-Focus Concentrator Arrays**. JX Crystals, Munich Conference.
- [Vonc00] VONCKEN, M. (2000) **The Development of a Mechanically Stacked InGaP – Si Tandem Solar Cell**. HELIOZ Project, University of Nijmegen/Netherlands Energy Research Foundation.
- [Stan00] STAN, M, AIKEN, D., SHARPS, P., HILLS, J., CLEVINGER, B. y FATEMI, N. **The Development of >28% Efficient Triple-Junction Space Solar Cells at Emcore Photovoltaics**. Emcore Photovoltaics.
- [Wolf98] WOLFE W (1998) **Introduction to Radiometry**. Tutorial Texts in Optical Engineering, Volume TT29, Spie Press.
- [Jasp97] JASPRIT, S. (1997) **Semiconductor Devices: An Introduction**. McGraw-Hill.

- [Fsec01] Florida Energy Center (2001) **Test Methods for Photovoltaics Module Ratings** Florida Energy Center, FSEC-GP-68-01.
- [Stan00] STAN, M., AIKEN, D., SHARPS, P., FATEMI, N., SPADAFORA, F., HILLS, J., YOO, H., y CLEVINGER, B. **27.5% Efficiency InGaP/InGaAs/Ge Advanced Triple Junction (ATJ) Cells for High Volume Manufacturing**. Emcore Photovoltaics.
- [Macm00] MACMILLAN, H., HAMAKER, H., VIRSHUP, G., y WERTHEN, J. **Multijunction III-V Solar Cells: Recent and Projected Results**. Varian Research Center.
- [Schw93] SSCHWARTZ, R. (1993) **Photovoltaic Power Generation**. Proceedings of the IEE, Vol 81, N°3.
- [Nrel05] NREL (2005) **PV Performance: Cells: Current-Voltage, Quantum Efficiency**. Energy Efficiency and Renewable Energy, US department of Energy. [http://www.eere.energy.gov/solar/performance\\_cells.html.3](http://www.eere.energy.gov/solar/performance_cells.html.3)
- [Burn02] BURNETT, B. (2002) **The Basic Physics and Design of III-V Multijunction Solar Cells**. NREL's III-V research group.

**APPENDIXES**

## APPENDIX A: RECOMBINATION PROCESSES IN SEMICONDUCTORS

Whereas high absorption of light in solar cell material is desired, recombination should be avoided. Recombination is the relaxation from electrons back to the valence band, without contributing to the solar cell power. Three mechanisms can be distinguished that can occur in parallel, in which case the recombination rate is just the sum of those for the individual processes. Radiative recombination is just the reverse of absorption. An electron relaxes from conduction band to valence band by emitting a photon with an energy, equal to the bandgap width. This form of recombination is the strongest in direct bandgap materials for the same reason, absorption is the largest in these materials.

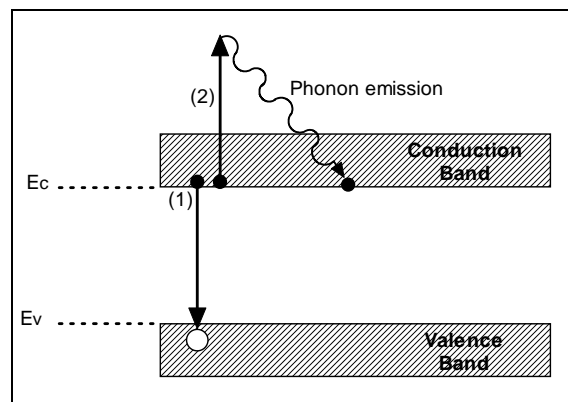


Figure A.1: Auger recombination with associated excess energy given to an electron in the conduction band: In the recombination process, the electron collides with another electron in the conduction band (1). After that, the second electron gains energy which is then dissipated as a phonons (2), no light is emitted.

Auger recombination is a process, in which an electron, when recombining with a hole collides with a another electron. Therefore, it transfers its excess energy to a second electron, instead of emitting light. The electron that receives the energy can be in the valence band or in the conduction band. It gains in energy, and relaxes to its original position by emitting phonons. The corresponding energy diagrams are shown in Figure A.1. Auger recombination is doping

concentration dependant: the higher the doping concentration, the higher the recombination. In good quality indirect bandgap materials with doping concentrations in excess of  $10^{17} \text{ cm}^{-3}$ , Auger recombination is the dominant recombination process.

Recombination through traps is caused by impurities and defects in the semiconductor material, which create allowed energy states in the forbidden bandgap. These defect levels enable a very efficient two-step recombination process, in which electrons relax from conduction band energies to the defect level and then relax to the valence band, annihilating a hole as shown in Figure A.2.

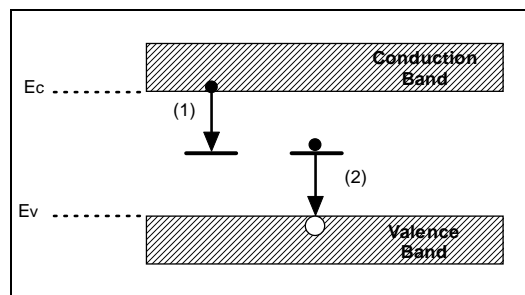


Figure A.2: Two step recombination process via a defect energy level, situated in the forbidden gap. The electron relaxes to an intermediate defect energy level (1), then recombines with a hole in the valence band (2)

Since a crystal boundary is in fact a very large defect, a lot of allowed defect levels are created in the forbidden bandgap near a crystal surface (see Figure A.3). These surfaces therefore act as very efficient recombination centers. For III-V materials, generally a lattice matched wide bandgap window layer is applied. This avoids the absorption of photons too close to the front surface leading to large surface recombination. By this layer, the lattice at the emitter surface is continued, so that no defect states occur in this region, while the carriers are kept away from the actual surface of the solar cell.

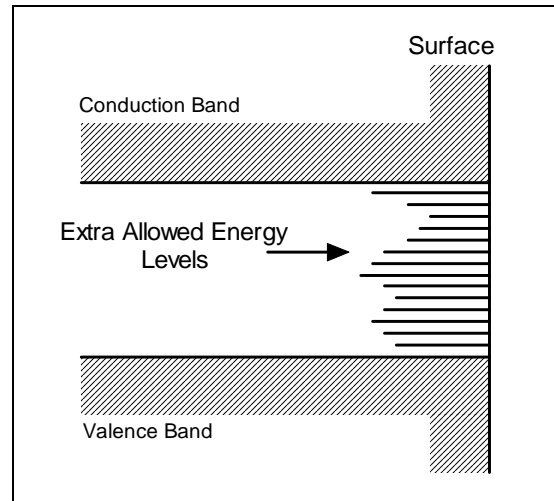


Figure A.3: Surface states lying within the forbidden bandgap at the surface of a semiconductor

## APPENDIX B: ABSORPTION IN DIRECT BANDGAP AND INDIRECT BANDGAP MATERIALS

In the energy–momentum diagram the valence and conduction band can be determined, as well as the forbidden bandgap. If the minimum of the conduction band is positioned exactly above the maximum in the valence band, the material is referred to as a direct-bandgap material. Photons with energies larger than the bandgap energy, that have entered the material, can provide an electron with enough energy to make the transition from valence to conduction band. The schematical band diagram of a direct bandgap material is given in Figure B.1

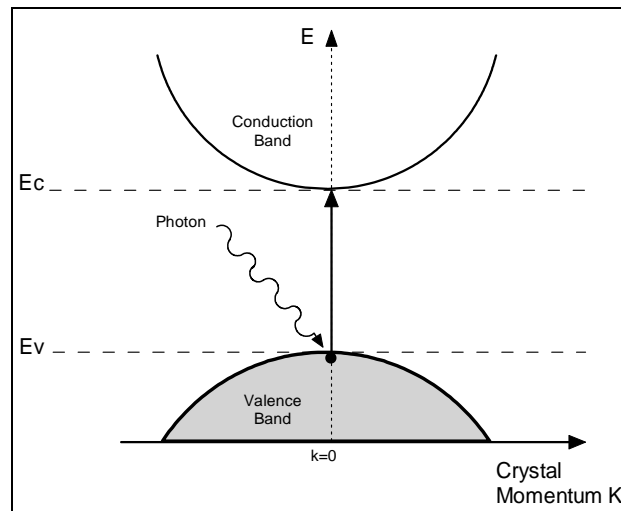


Figure B.1: Schematical energy-momentum diagram for a direct bandgap material

If the minimum of the conduction band is not positioned above the maximum of the valence band in the energy–momentum diagram (see Figure B.2), an additional momentum difference has to be over won, before the transaction from valence to conduction band by electrons can take place (indirect bandgap materials). This momentum difference is provided by quantized lattice vibrations or phonons. These phonons have low energy and high momentum, whereas photons have high

energy and low momentum. If an electron acquires enough energy to make the required transfer to the conduction band, the absorption of a phonon can provide the necessary momentum to actually reach the conduction band. A schematical diagram, displaying the transition of an electron from valence to conduction band by phonon absorption is given in Figure B.2. Since photons are much easier absorbed in a direct bandgap material, solar cells made of these materials can be much thinner.

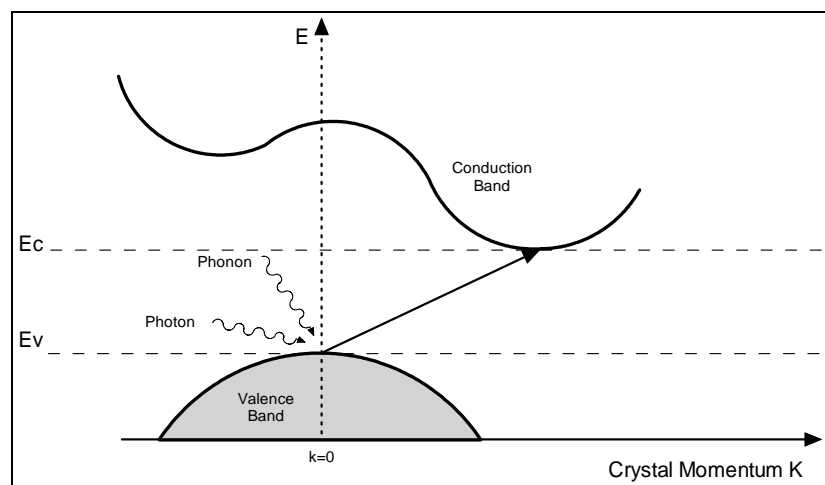


Figure B.2: Schematical energy-momentum diagram for an indirect bandgap material

Silicon (Si) and Germanium (Ge) are both indirect bandgap semiconductors. Figure B.3, displays the energy-momentum diagram of the silicon semiconductor where  $E_g$  is the bandgap. Semiconductors such as GaAs, InAs, InP are direct bandgap semiconductors.

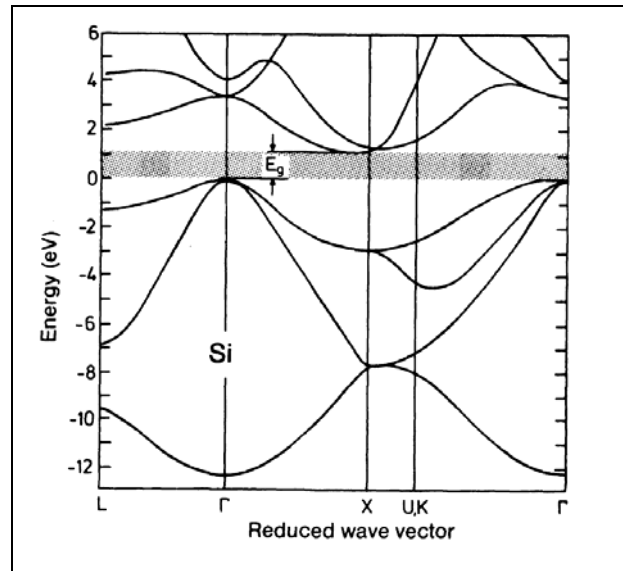


Figure B.3: Energy-momentum diagram for silicon